Journal of Marine Research, 56, 1163–1201, 1998

Journal of
MARINE RESEARCH

Volume 56, Number 6

Tidal mixing and cross-frontal particle exchange over a finite amplitude asymmetric bank: A model study with application to Georges Bank

by Changsheng Chen[1] and Robert C. Beardsley[2]

ABSTRACT

Tidal mixing, internal wave bores, and cross-bank particle transport over a finite amplitude asymmetric bank are examined using a two-dimensional primitive equation ocean model with Mellor and Yamada (level 2.5) turbulent closure. Driven by the surface M_2 tide, the model results show that tidal mixing exhibits temporal and spatial asymmetries on southern and northern flanks of the bank. It is strongest near the bottom around maximum on-bank tidal flow as a result of gravitational instability when denser water is advected upslope over lighter water. A sharp thermal depression occurs on the steep northern flank, which produces large current shear and strong tidal mixing throughout the upper 50 m of the water column. Dissipation also exhibits a strong tidal variation, with the largest values (of order 10^{-5} W/kg) occurring near-bottom around maximum on- and off-bank tidal flow. Dissipation generally decreases upward, with a distinct phase lag in the vertical. Fluid particles are advected upslope near the bottom in the upper slope region (depth <150 m) on both flanks, with some particles moving across the tidal mixing fronts near the bottom. The near-bottom residual Lagrangian current is opposite in direction to the residual Eulerian current on the northern flank due to strong nonlinearity over the steep bottom slope. The mean upslope advection of fluid particles near the bottom on both flanks is consistent with model passive tracer experiments, suggesting that strong tidal forcing of a stratified fluid over the bank can provide one physical mechanism responsible for high concentrations of nutrients and hence phytoplankton at the fronts on Georges Bank. The model predictions of eddy viscosity and turbulent dissipation rates are in good agreement with estimates based on recent current and microstructure measurements made on Georges Bank.

1. Department of Marine Sciences, The University of Georgia, Athens, Georgia, 30602-2206, U.S.A.
2. Department of Physical Oceanography, Woods Hole Oceanographic Institution, Woods Hole, Massachusetts, 02543, U.S.A.

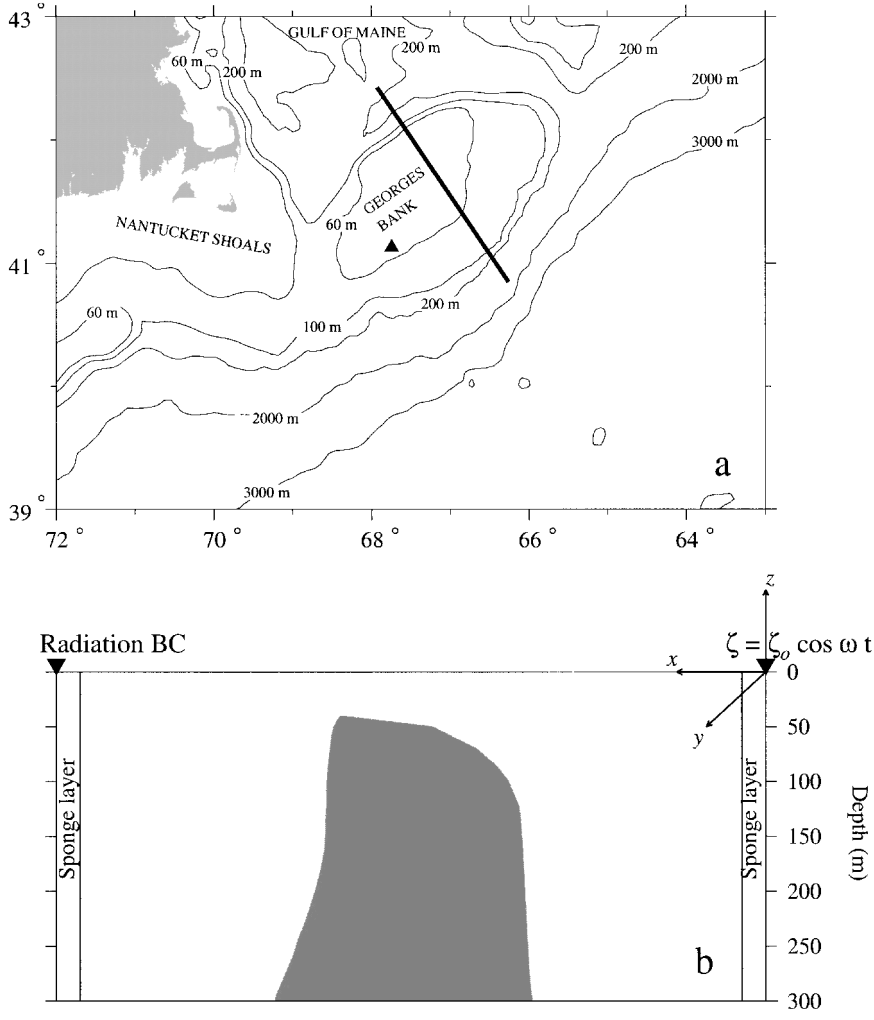

Figure 1. Bathymetry (in meters) of the southern New England continental margin (a) and a cross section of the 2-D model domain (b). In (a), the heavy solid line and filled triangle indicate the locations of the cross-bank section used in numerical experiments (A, B, and C) and anchor measurement stations (D-H). The model is forced by the M_2 surface tide at the southern open boundary on the right. A radiation boundary condition plus a sponge layer are imposed at the northern open boundary on the left. The sponge layer at the southern open boundary is only applied to the current field.

1. Introduction

The water motion over Georges Bank (Fig. 1) is controlled dominantly by strong M_2 tidal currents. These currents exhibit a rotary character over the bank and increase as the water becomes shallower. The maximum velocity is about 30 cm/s near the shelf break on

the southern flank and about 100 cm/s at the edge of the northern flank (Moody *et al.,* 1984). Tidal-induced turbulent mixing across this finite-amplitude, asymmetric bank varies temporally and spatially and is closely related to the dynamics of the sloping bottom boundary layer (Loder *et al.,* 1992; Chen *et al.,* 1995; Horne *et al.,* 1996; Yoshida and Oakey, 1996). Physical processes controlling the sloping bottom boundary layers on the northern and southern flanks differ due to the large difference in bottom slope. These dynamics are not well understood.

Strong tidal mixing creates a well-defined tidally mixed front (TMF) around the shallow cap of Georges Bank. This TMF acts like a barrier separating well-mixed water on the top of the bank from stratified water on the flanks. During late spring through summer, the TMF is located near the 40-m isobath on the northern flank and about the 60-m isobath on the southern flank (Flagg, 1987; Chen *et al.,* 1995). During winter, the TMF disappears over the southern flank as strong wind mixing and surface cooling homogenize the local water column.

The kinematics of cross-frontal water exchange over Georges Bank have been only partially examined. For the weak nonlinear case in which the cross-isobath tidal excursion length is much shorter than the cross-isobath variation scale of the Eulerian velocity, the Euler-Lagrange transformation can be expanded in the form of a Taylor series. In this case, the Lagrangian velocity of a fluid parcel is approximately equal to the sum of Eulerian and Stokes velocities. Here the Stokes velocity is defined as the first derivative term of the Taylor series expansion of the Euler-Lagrange transformation (Longuet-Higgins, 1969; Zimmerman, 1979; Loder, 1980). Based on this assumption, Loder and Wright (1985) used a 2-D model to estimate the cross-frontal Lagrangian residual current over Georges Bank and found the predicted Lagrangian flow pattern was similar to the Eulerian flow on both northern and southern flanks. They also noted that their model results may not apply for Georges Bank because of the likely effect of high-order terms in the Taylor expansion. The real circulation over the bank is controlled by tidal rectification processes associated with strong nonlinearity (Loder, 1980; Chen *et al.,* 1995). For example, on the northern flank, the cross-isobath variation scale of the Eulerian velocity is about 10 km or less, which is equal to or less than the tidal excursion length (10 km or more), invalidating the key assumption for the Taylor expansion of the Euler-Lagrange transformation. Thus, important and unanswered questions arise about how fluid particles move across topography in the strongly nonlinear flow regime over Georges Bank.

The northern flank of Georges Bank has been identified as a location of complex strong internal waves (Loder and Horne, 1991; Loder *et al.,* 1992; Marsden, 1986). Internal tides are generated through the interaction of the barotropic tides with the variable bottom topography (Wunsch, 1969; Baines, 1982; Chen and Beardsley, 1995). In the deep region away from the bank, the internal tidal flow is always subcritical. Over the northern flank and top of the bank, however, it can be supercritical during flood and ebb tides and subcritical near the tidal transition. The existence of two critical states over the bank suggests that a hydraulic jump or lee wave may occur at the lee side of the bank during the

local ebb tide (Farmer and Smith, 1980; Pratt, 1991; Loder *et al.,* 1992). The off-bank tidal current tends to prevent the internal waves from propagating on-bank, causing an accumulation of wave energy on the lee side of the bank during ebb tide. The accumulated wave energy propagates on-bank when tidal currents reverse during local flood tide (Maxworthy, 1979).

Internal wave generation over the northern flank of Georges Bank has been examined by Lamb (1994). Using a two-dimensional, nonhydrostatic model, he reproduced the development of a large internal density depression over the northern flank during off-bank flow, with subsequent on-bank internal wave propagation and steeping as the tidal current turned on-bank. However, the model was inviscid, the numerical computation became unstable after just a few tidal cycles, and the relationship between internal wave generation and tidal mixing remains unexplored.

As observational components of the US Global Ecosystem (GLOBEC) Georges Bank Program, multiple instruments such as Conductivity-Temperature-Depth (CTD), Vector Measuring Current Meters (VMCMs), a Benthic Acoustic Stress Sensor (BASS) tripod, Acoustic Doppler Current Profiler (ADCP), and the microstructure profiler, were deployed on the southern flank of Georges Bank to measure currents, temperature, and salinity within the bottom boundary layer (Werner, 1996; Burgett *et al.,* 1996; Burgett, 1997). Similar field measurements were made on the northern flank of Georges Bank by Canadian scientists (Yoshida and Oakey, 1996; Horne *et al.,* 1996). These measurements have provided the detailed vertical microstructure of turbulence kinetic energy, mixing, and dissipation, and also given us an opportunity to identify, qualify, and quantify the physical processes controlling tidal mixing over Georges Bank.

In this paper, we examine tidal mixing, internal wave generation, and cross-bank particle transport over a finite-amplitude bank using a two-dimensional version of the Blumberg and Mellor (1987) numerical primitive-equation coastal ocean circulation model with Mellor and Yamada level 2.5 turbulent closure (see Chen and Beardsley, 1995 (denoted C&B) for a detailed description of the 2-D model). The model domain represents an idealized cross-bank slice of Georges Bank, with no along-isobath variation allowed. Using this 2-D approach facilitates numerical experiments with high resolution, which is recognized as critically important in particle tracking and bottom boundary layer simulation (Zimmerman, 1979; C&B). Recently, we have developed a fully 3D model of the Gulf of Maine/Georges Bank region. Comparison of the 2-D and 3-D model results for the case of tidal spin-up with summer stratification shows good agreement in the structure of the tidal mixed front, along-front residual current, and secondary cross-frontal circulation along the 2-D model cross-bank section. This supports the use of the 2-D model to study specific processes in an idealized setting.

The remaining sections of this paper are organized as follows. Section 2 describes the physical model and Lagrangian particle tracking approach. Section 3 presents the model results of turbulent mixing and dissipation across the bank and comparison with recent field measurements. Section 4 describes the internal waves over the southern and northern

flanks. In Section 5, the trajectories of particles released at different locations across the bank are used to study the cross-frontal exchange of water masses and marine organisms. An alternative study using a dissolved passive tracer is included to compare with the particle trajectories. An additional discussion on the up-slope water transport and turbulent closure model is given in Section 6, and conclusions are summarized in Section 7.

2. The physical model

The physical model used in this study is a modified 2-D version of the Blumberg and Mellor (1987) prognostic coastal ocean circulation model (C&B). This model includes a free surface and parameterization of vertical mixing using the Mellor and Yamada (1974, 1982) level 2.5 (MY-2.5) turbulent closure scheme as modified by Galperin *et al.* (1988). To better understand the dynamics of the turbulent mixing presented in this paper, we give next a brief description of the MY-2.5 turbulent closure model.

In the boundary layer approximation where the shear production of turbulent kinetic energy is assumed to be produced by vertical shear of the horizontal flow near the boundary, the 2-D equations for q^2 and q^2l can be simplified to

$$(q^2)_t + u(q^2)_x + w(q^2)_z = 2(P_s + P_b - \varepsilon) + (K_q(q^2)_z)_z + F_q \tag{1}$$

$$(q^2l)_t + u(q^2l)_x + w(q^2l)_z = 1.8l(P_s + P_b - 0.56\varepsilon W) + (K_q(q^2l)_z)_z + F_l \tag{2}$$

where $q^2 = (u'^2 + v'^2)/2$ is the turbulent kinetic energy, l the turbulent macroscale, K_q the vertical eddy diffusion coefficient of the turbulent kinetic energy, F_q and F_l represent the horizontal diffusion of the turbulent kinetic energy and macroscale, $P_s = K_m(u_z^2 + v_z^2)$ and $P_b = (gK_h\rho_z)/\rho_o$ the shear and buoyancy production terms of turbulent kinetic energy, $\varepsilon = 0.06q^3/l$ the turbulent kinetic energy dissipation rate, $W = 1 + 1.33l^2/(\kappa L)^2$ a wall proximity function where $L^{-1} = (\zeta - z)^{-1} + (H + z)^{-1}$, $\kappa = 0.4$ the von Karman constant, H the mean water depth, and ζ the free surface elevation. In general, F_q and F_l were kept as small as possible to reduce the effects of horizontal diffusion on the solutions.

The turbulent kinetic energy and macroscale equations are closed by defining

$$K_m = lqS_m, \qquad K_h = lqS_h, \qquad K_q = 0.2lq. \tag{3}$$

S_m and S_h are defined as the stability functions

$$S_m = \frac{0.39 - 3.89G_h}{1 - 34.68G_h(1 - 10.1G_h)}, \qquad \text{and} \qquad S_h = \frac{0.49}{1 - 34.66G_h}, \tag{4}$$

where $G_h = [(l^2g)/(q^2\rho_o)]\rho_z$. In the original MY level 2.5 turbulent closure model (Mellor and Yamada, 1974, 1982), S_m and S_h were functions of the gradient Richardson number. By removing a slight inconsistency in the scaling analysis, Galperin *et al.* (1988) simplified the MY turbulent closure model so that S_m and S_h depend only on G_h. G_h has an upper bound of 0.023 for the case of unstable ($\rho_z > 0$) stratification and with a lower bound of -0.28 for the case of stable ($\rho_z < 0$) stratification. As in C&B, the surface and bottom boundary

conditions for the turbulent kinetic energy and macroscale equations are

$$q^2 = q^2 l = 0 \quad \text{at} \quad z = \zeta, \qquad q^2 l = 0, \qquad q^2 = B_1^{2/3} u_{\tau b}^2 \quad \text{at} \quad z = -H, \tag{5}$$

where $u_{\tau b}$ is the friction velocity associated with the bottom stress and B_1 an empirical constant equal to 16.6. The boundary conditions for velocities and temperature are given in details in C&B.

The numerical domain featured a cross-bank section cut from southeast to northwest across the center of Georges Bank (Fig. 1). The water depth varied from 300 m off the bank to 100 m at the southern shelf break, and then gradually decreased to 40 m at the northern edge of the bank. The numerical model used the σ-coordinate transformation defined by $\sigma = (z - \zeta)/(H + \zeta)$ where σ varied from 0 (at the surface) to −1 (at the bottom). A uniform grid was used in σ, with vertical resolution $\Delta\sigma = 0.011$ (91 points in the vertical). This resolution corresponds to a maximum vertical Δz of 3.3 m off the bank and to 0.44 m at the northern flank. A nonuniform horizontal grid was used in the cross-bank direction. The horizontal Δx was 500 m near and across the bank and increased linearly over an interval of 30 grid points to 11.96 km outside the domain of interest. The model time step was 110.4 sec, corresponding to 405 time steps over a M_2 (12.42 hr) tidal cycle.

Particle trajectories were traced by solving the x and z velocity equations

$$\frac{dx}{dt} = u, \qquad \frac{d\sigma}{dt} = \frac{\overline{\omega}}{H + \zeta}, \tag{6}$$

where u and $\overline{\omega}$ are the x and σ components of water velocity, respectively. The relation between $\overline{\omega}$ and w is defined as

$$\overline{\omega} = w - (1 + \sigma)\frac{d\zeta}{dt} - \sigma\frac{dH}{dt} \tag{7}$$

where w is the vertical velocity in the z coordinate direction. The kinematic equations for u and $\overline{\omega}$ were calculated by means of a fourth-order Runge-Kutta scheme with a truncation error of order $(\Delta t)^5$. Particle velocities used in this calculation were obtained using a bilinear interpolation from the four nearest grid points. At each time step, each particle was checked to see if it was located inside the numerical domain. If a particle hit the bottom, it was reinitialized to a new position using the theory of wave reflection on the slope where the angle of reflection equaled the angle of incident. An alternative method, which was to keep the particle at the bottom once it moved out of the model domain, was also tested in our numerical experiments. No significant differences between these two methods were found for those cases in which high vertical resolution was used.

The fourth-order Runge-Kutta method requires that the time step Δt is chosen to satisfy the criterion $\Delta t K < 0.05$, where K is an upper bound of the spatial gradient of velocity. In our numerical experiments, K can be approximated by ω (the M_2 tidal frequency), which yields $\Delta t\omega \approx 0.016$ for $\Delta t = 110.4$ sec, a much smaller value than the above criterion. We

tracked particles in the model space (x, σ) and then converted their trajectories back to the physical space (x,z). This method avoids the interpolation errors due to repeated transformations from the σ- to the z-coordinate.

Since the flow is nondivergent in the cross-bank plane, the cross-bank velocity field can be described by a streamfunction defined as

$$\psi = -\int_H^z u dz, \tag{8}$$

which satisfies $u = -\psi_z$ and $w = \psi_x$.

The model was forced by the barotropic M_2 tidal elevation at the southern open boundary. A gravity wave radiation boundary condition plus a sponge layer was specified at the northern open boundary to allow the tidal wave to propagate out of the computational domain with minimum reflection (Chapman, 1985). To simulate summertime stratification, the initial temperature distribution was specified as a linear function of z, with a temperature of 20°C at the surface and 11°C at the bottom. To simplify the numerical experiments and interpretation of model results, a constant salinity of 35 PSU was chosen throughout the model domain, so that the model density depended solely on temperature. To minimize the transient response to sharp initial forcing, the boundary tidal forcing was initially ramped up to its full value over two tidal cycles, and the model integration continued in time until a periodic quasi-equilibrium state was attained, typically after about 20 tidal cycles (C&B). The residual fields of current and temperature presented here are taken from the periodic quasi-equilibrium state.

3. Features of tidal mixing

a. Tidal currents, tidal mixing fronts and residual currents

For the case of strong (summer) stratification, the periodic equilibrium state is characterized by strong rotary M_2 tidal currents over the bank, with a maximum cross-bank surface current of about 100 cm/s at the bank crest. The model M_2 tidal ellipse has a ratio of major axis to minor axis of 1.44–1.48, consistent with the theoretical value of $\omega/f = 1.47$ for a Sverdrup plane wave propagating across the bank (Brown, 1984). The model M_2 major axis is oriented about 1 to 3° counter-clockwise from the on-bank direction, so that the cross-bank component of current is a good approximation for the tidal current along the major axis. The model M_2 tidal current vector leads in time as the bottom is approached; i.e., the current vectors at all levels rotate anticyclonically (clockwise) with an offset of the current vector near the bottom as a result of the bottom friction. Thus, the transition between on- and off-bank flows occurs first in time at the bottom.

The increased tidal mixing over the top of the bank creates the TMFs near the 50 to 60-m isobath on the southern flank and the 40-m isobath on the northern flank (Fig. 2a). These fronts separate vertically, well-mixed water over the top from stratified water over the flanks. The presence of stratification increases the cross-bank density gradient near these fronts, enhances cross-bank tidal current advection (stratified tidal rectification), and

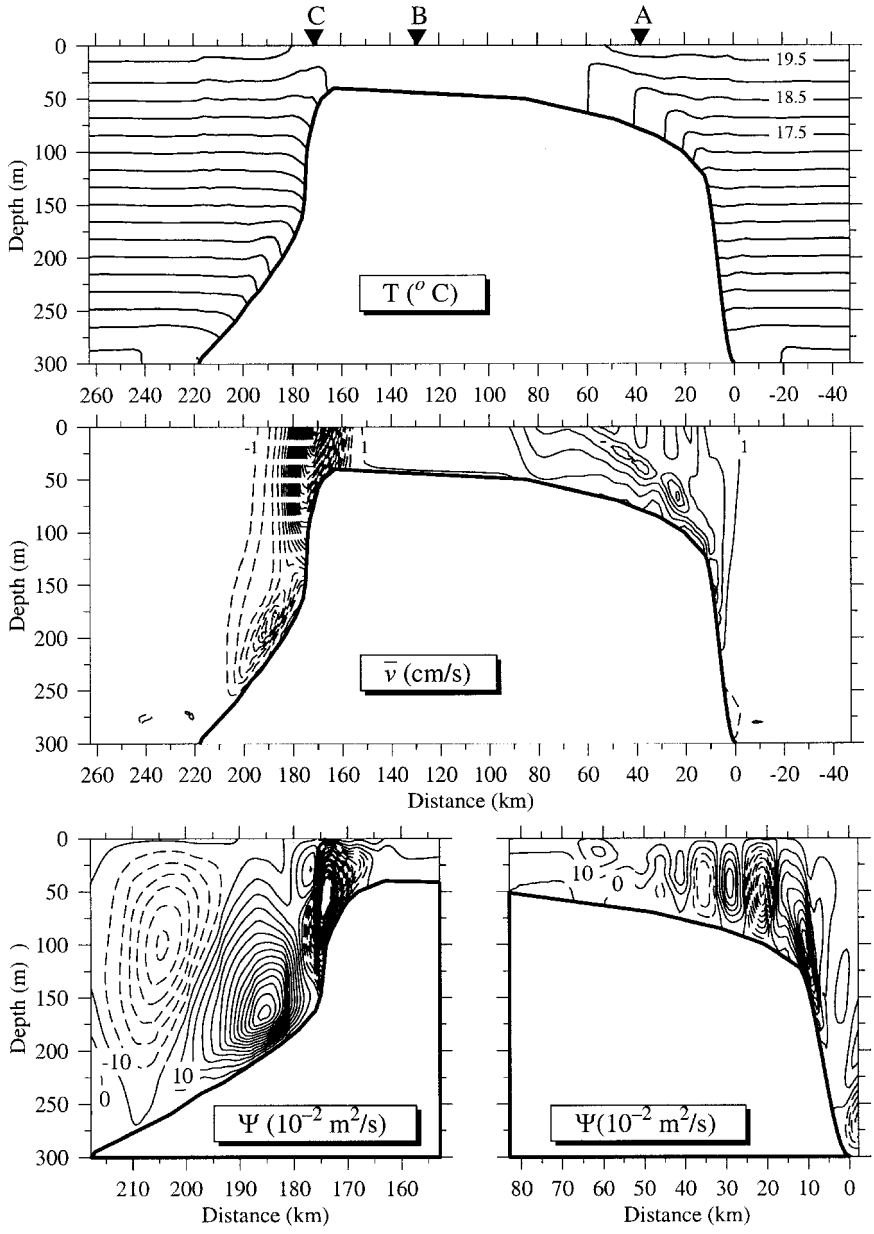

Figure 2. Cross-bank distributions of temperature, along-bank velocity, and cross-bank streamfunction averaged over a tidal cycle on the 15th model day for the case of summer stratification. Filled downtriangles labeled A, B, and C indicate the sites where the time-dependent behavior is examined in detail. The southern flank, crest, and northern flank sites correspond to the following isobaths: A-78 m; B-44 m; and C-67 m. In (b): the direction of the along-bank residual current is indicated by symbols at the top of the figure. In (c): the direction of the cross-bank residual current is indicated by arrows on the streamlines.

reduces internal friction (C&B). As a result, the along-bank residual current is intensified at fronts. On the northern flank, the maximum along-isobath current increases from 16 cm/s in the case of no stratification (Chen *et al.,* 1995) to 32 cm/s in the case of summer stratification presented here. On the southern flank, the along-isobath residual current intensifies at the top of the bottom mixed layer, with a maximum along-isobath current of 8 cm/s at a height of 27 m above the bottom at the front (Fig. 2b).

The model-predicted pattern of secondary cross-bank circulation varies significantly with different bottom slopes and tidal mixing. On the northern flank, the model predicts double closed circulation cells, with horizontal divergence near the surface and convergence near the bottom at the edge of the front and a near-surface convergence in the stratified region near the front (Fig. 2c). The residual Eulerian velocity near the sloping bottom is characterized by an off-bank downwelling current with a maximum velocity of 10 cm/s in the horizontal and 0.3 cm/s in the vertical. On the southern flank, the secondary circulation is characterized by multiple closed cells within the frontal zone between the 50-m and 100-m isobaths. The cross-bank and vertical residual velocities vary in a range of 0.5–3 cm/s and of 0.01–0.05 cm/s, respectively (Fig. 2c).

b. Vertical eddy viscosity

In the MY 2.5 level turbulent closure model, the vertical eddy viscosity, K_m, is determined by a product of the turbulent kinetic energy q, the turbulent macroscale l, and the stability function S_m (Eqs. 3 and 4). Here q and l are functions of the magnitude of the vertical current shear and vertical gradient of density (here temperature), while S_m depends on the vertical density gradient. Tide-induced shear production of turbulent kinetic energy, P_s, exhibits maximum values near the bottom due to the large vertical shear caused by bottom friction. Since bottom friction increases with the magnitude of the tidal currents, the shear production should be largest where the cross-bank tidal current component is largest. The buoyancy production of turbulent kinetic energy, P_b, depends on the local vertical gradient of temperature ($P_b \propto -\partial T/\partial z$). As a result of combined shear and buoyancy productions, the vertical eddy viscosity K_m should vary markedly with space and time over the bank during flood and ebb tidal cycles. We will now describe the time-dependent behavior of K_m and other variables at three representative sites (A–C) over the bank (Fig. 2).

Southern flank (site A). On the southern flank, at the 78-m isobath (site A), strong turbulent mixing occurs only in the bottom boundary layer, a 25 to 30-m thick layer with weak stratification (Fig. 3). In this layer K_m varies periodically with the magnitude and direction of cross-bank tidal current, with a maximum $K_m \approx 0.04$ m^2/s occurring within one hour after maximum on-bank tidal current (40 cm/s) and a minimum $K_m \approx 0.015$ m^2/s occurring around tidal transition.

The stability function $S_m (= K_m/ql)$ also exhibits a similar asymmetry in time, with a maximum value of 0.5 near the bottom about 1 to 2 hours after the maximum K_m. Due to the rotary nature of these tidal currents, q exhibits two maxima during each tidal cycle.

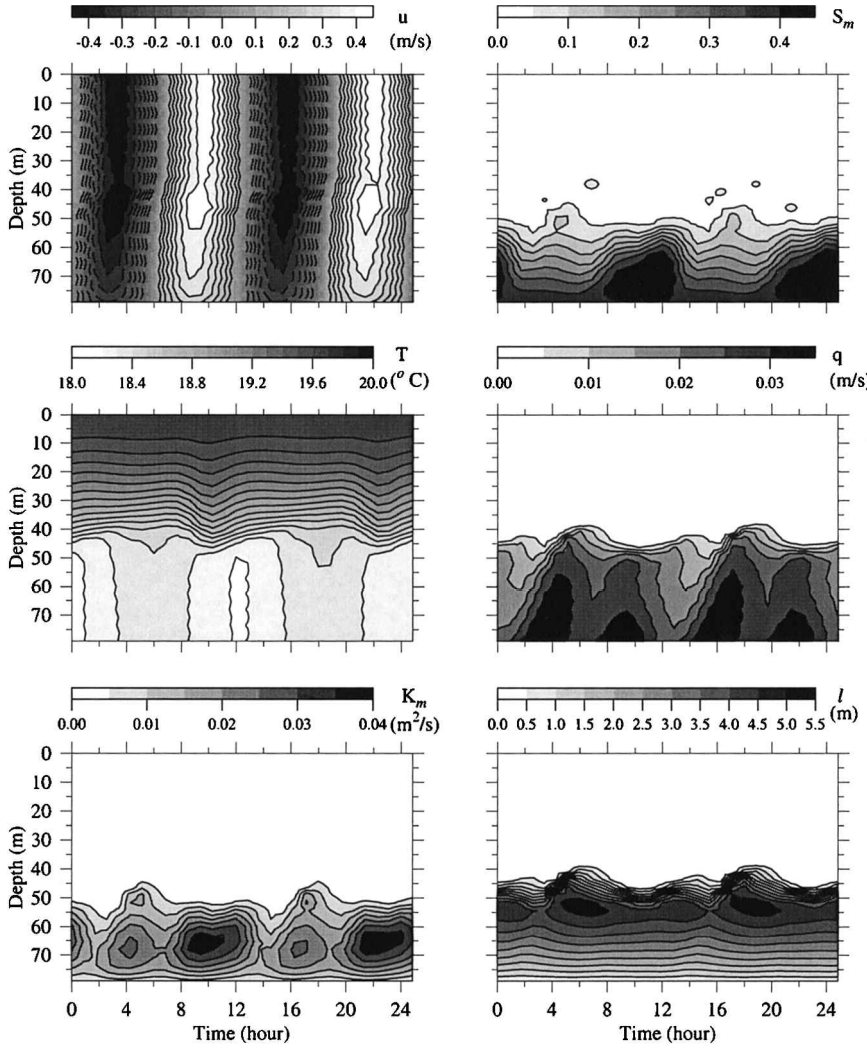

Figure 3. Time series of cross-bank current (u), temperature (T), vertical thermal diffusion coefficient (K_m), stability function (S_m), square root of turbulent kinetic energy (q), and turbulent macroscale (l) over two tidal cycles at site A on the southern flank.

During on-bank flow, the largest value of q occurs within a layer of 10 m starting from the bottom, while during off-bank flow, it extends upward to cover a layer of 20 to 25 m above the bottom. The macroscale l also varies periodically and has a maximum value of 5 m at tidal transition. The largest value of l occurs at a height of 25–30 m above the bottom in the upper part of the bottom mixed layer.

One striking feature at this site is that the largest q occurs during off-bank flow and the largest l at tidal transition. With $K_m = qlS_m$, it is clear that the weaker secondary maximum

in K_m during off-bank flow is due to the smaller values of S_m and l but not q (which was at its maximum), while the primary maximum of K_m during the on-bank flow is due to an enhanced S_m plus increased ql.

What is the explanation of this asymmetric behavior of tidal mixing according to the model physics? As seen in the temperature time series (Fig. 3), the temperature in the bottom boundary layer decreases during on-bank flow. Due to the strong shear of the cross-bank current near the bottom, the temperature drops more rapidly in the upper part of the boundary layer than near the bottom, as cooler water is preferentially carried over the warmer water nearest the bottom. This results in gravitational instability near the bottom in a period of about 3 to 4 hours during on-bank tidal flow. The unstable vertical profile of temperature produces a positive P_b, increases S_m, and thus enhances K_m. During off-bank flow, the vertical shear of the tidal current causes the water to warm up more slowly near the bottom than in the upper part of the boundary layer, enhancing vertical stratification and reducing vertical mixing.

Crest (site B). Over the top of the bank between TMFs, the water is vertically well mixed (Fig. 2) and K_m is characterized by a parabolic curve in the vertical, which varies in magnitude as a function of the magnitude of the cross-bank tidal current. At the 44-m isobath (site B), K_m has a maximum value of about 0.07 m^2/s at a depth of 25 m, decreasing upward to the surface and downward to the bottom (Fig. 4). K_m varies almost symmetrically in time, with its maximum value occurring about one hour after maximum on- and off-bank currents.

The symmetric variation of K_m over the crest is a result of the basic rotary nature of the M_2 tidal current. In this well-mixed region, turbulent kinetic energy is produced by shear production. Since shear production is independent of the current direction, the variation of q is nearly symmetric in time through flood and ebb tidal cycles. l is largest around mid-depth and decreases toward both surface and bottom boundaries. This contributes directly to the largest value of K_m found at mid-depth about one hour after maximum flood and ebb currents.

Northern flank (site C). On the northern flank at the 67-m isobath (site C), K_m and other variables exhibit much more complex time-dependent patterns (Fig. 5). The cross-bank current is asymmetric in time, with a faster (slower) off-bank (on-bank) flow over a shorter (longer) time interval (Figs. 5 and 7). The off-bank current also exhibits a significant O(1 hour) time lag in the vertical, which is not seen in the on-bank flow. During off-bank flow, mixing is moderate in strength and restricted in a thin bottom boundary layer of 5–10 m during the initial phase. Just after maximum off-bank flow, the temperature within the upper 50 m reverses its warming tendency and remains cooler with a much reduced vertical density gradient for about two hours. This produces a large K_m of about 0.01–0.04 m^2/s in the upper 50 m.

During on-bank tidal flow, the temperature within the lower 50 m above the bottom

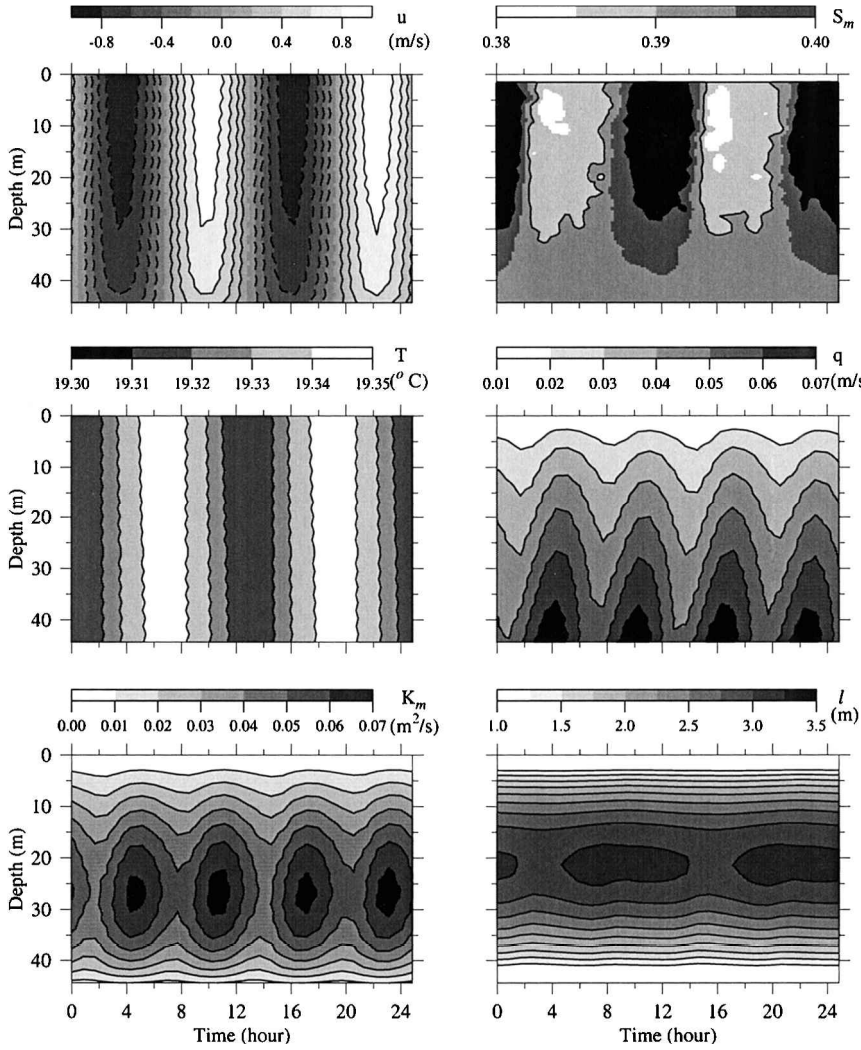

Figure 4. Time series of cross-bank current (u), temperature (T), vertical thermal diffusion coefficient (K_m), stability function (S_m), square root of turbulent kinetic energy (q), and turbulent macroscale (l) over two tidal cycles at site B at the crest of the bank.

decreases monotonically as the on-bank tidal current increases, with a cold core forming near the bottom about one hour after maximum on-bank flow. Near the bottom, tidal mixing also increases upward as the on-bank flow increases, with a maximum K_m of about 0.04 m^2/s occurring at a depth of about 58 m (8 m above the bottom), about one hour before maximum on-bank flow.

At site C, q generally decreases with height above the bottom, with the largest value near

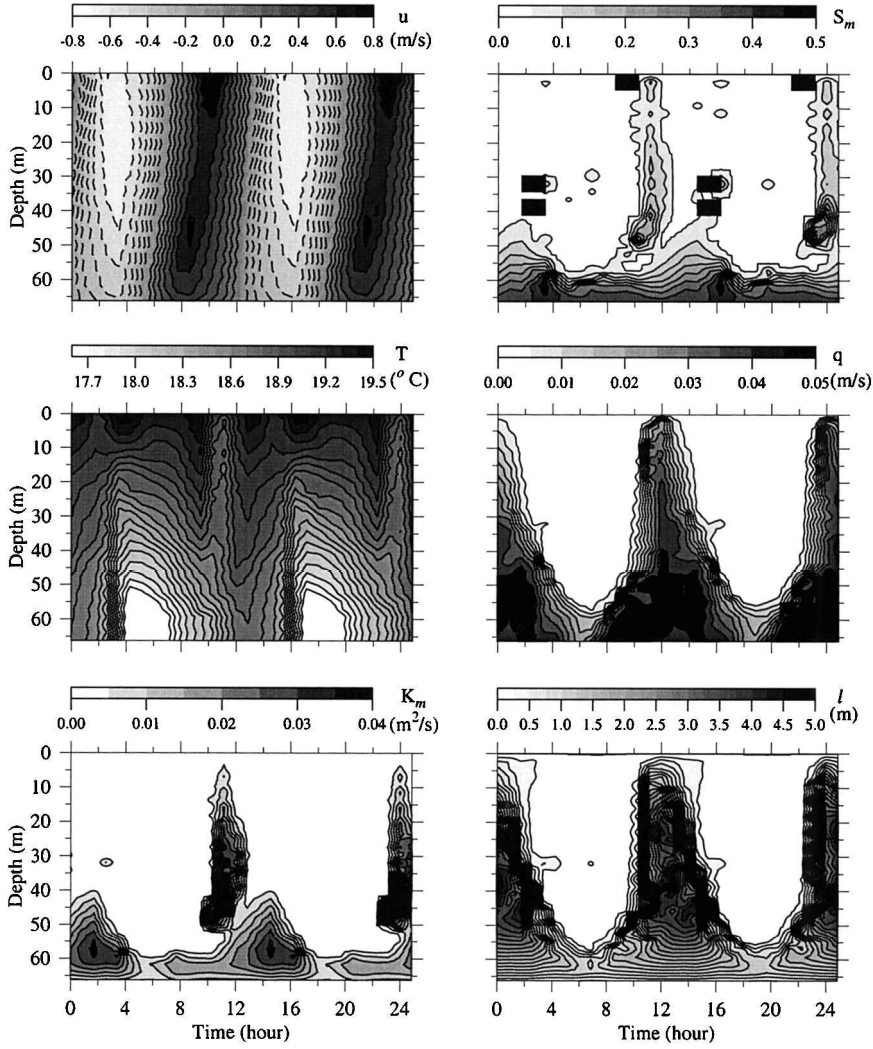

Figure 5. Time series of cross-bank current (u), temperature (T), vertical thermal diffusion coefficient (K_m), stability function (S_m), square root of turbulent kinetic energy (q), and turbulent macroscale (l) over two tidal cycles at site C on the northern flank.

the bottom between off-bank and on-bank flows. This temporal pattern is significantly different from that observed over the crest or southern flank where q has two maxima per tidal cycle. Corresponding to the occurrence of the cold water column in the upper 50 m during off-bank tidal flow, q, S_m, and l increases quickly about one hour after maximum off-bank current and extends vertically to the surface. This leads to the large K_m formed in the upper 50 m water column after maximum off-bank flow.

Comparisons with observations and previous model results. The model-predicted asymmetry of tidal mixing during off- and on-bank tidal flows is evident in recent observations on the northeastern flank of Georges Bank. Combined CTD, ADCP, and microstructure measurements made at site D (Fig. 1) during summer–fall, 1988 showed a cold core of temperature near the bottom during on-bank flow, which resulted in relatively stronger tidal mixing occurring around maximum on-bank tidal current (Yoshida and Oakey, 1996). Microstructure measurements made in the bottom boundary layer at the shelf break in the East China Sea also showed stronger mixing as cold water was advected onto the shelf during flood tidal flow (Matsuno *et al.,* 1994).

Estimates of K_m have been made using *in-situ* data at several sites on Georges Bank. Using high resolution current profile data obtained at a weakly stratified site on the 75-m isobath (site E, Fig. 1) on the southern flank during February–March, 1995, Werner (1996) found that K_m increased to a maximum value of 0.06 ± 0.02 m^2/s at a height of 30 m above the bottom. Based on turbulent dissipation rate estimates and the mean vertical current shear observed during April–June, 1995, Burgett (1997) calculated the time-depth averaged K_m at a mixed site on the 45-m isobath (site F, Fig. 1) to be 0.032 ± 0.003 m^2/s (with a depth-averaged tidal range of 0.01 to 0.05 m^2/s with an uncertainty of ± 0.003 m^2/s, and at a stratified site on the 76-m isobath on the southern flank (site G, Fig. 1) to be 0.023 ± 0.004 m^2/s (with a depth-averaged tidal range of 0.003 to 0.044 m^2/s with an uncertainty of ± 0.004 m^2/s). A similar estimation made by Yoshida and Oakey (1996) showed that K_m was higher than 0.01 m^2/s near the bottom around maximum on-bank and off-bank flows at the stratified site D on the northern flank.

Model predictions of K_m are consistent with these recent field estimates. At site A, the model-predicted, time-depth averaged K_m in the bottom mixed layer was 0.023 m^2/s with a depth-averaged tidal range of 0.003 to 0.044 m^2/s. This value was in good agreement with Burgett's (1997) results at site F. At site C, the model predicted K_m near the bottom varied from 0.01 to 0.04 m^2/s, which was in the same range as the observed values estimated by Yoshida and Oakey (1996).

To compare with Werner's (1996) results, we re-ran the model with weaker initial stratification to simulate the winter case. At the 76-isobath on the southern flank, the model-predicted, tidally averaged K_m varies parabolically in the vertical, with a maximum value of 0.05 m^2/s at a height of 30 m above the bottom. This shape and amplitude compare well with Werner's profile over the lower half of the water column.

Naimie (1996) used a turbulent closure finite-element model to study the 3-D circulation over Georges Bank during weak and strong stratification periods. He also noticed a dense lens occurring near the bottom during the flood tide. Our model results, with an idealized stratification and bottom topography, support the similar finding by Naimie (1996) and also provide additional insights into gravitational instability related to enhanced tidal mixing around the maximum flood tide.

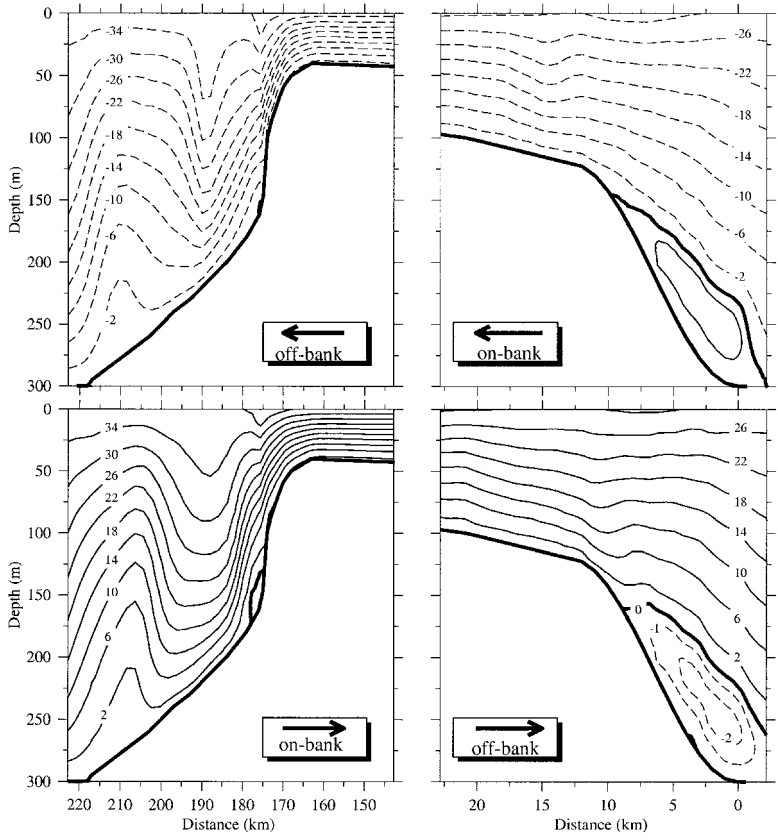

Figure 6. The cross-bank streamfunction Ψ at maximum flood and ebb tides on the southern (right) and northern (left) flanks. The contour interval for Ψ is 4 m^2/s.

c. Thickness of the bottom boundary layer

Physical processes controlling tidal mixing over the southern and northern flanks differ. On the southern slope during on-bank tidal flow, the interaction of the tidal current with the sloping bottom results in a counter-clockwise, cross-isobath circulation cell near the bottom below 150 m (Fig. 6). This current advects colder water upslope in the interior and warmer water downslope near the bottom, thus enhancing vertical mixing. When the tidal flow turns off-bank, the near-bottom, cross-isobath circulation cell reverses, advecting warmer water downslope in the interior and colder water upslope near the bottom and thus reducing vertical mixing. The thickness of the bottom boundary layer is defined here as the height above the bottom where $\Delta T = T(z) - T_b \leq 0.02$°C. Here $T(z)$ is the temperature at z and T_b is the temperature at the bottom (Lentz and Trowbridge, 1991; Trowbridge and Lentz, 1991). Over the upper flank in water depths less than 150 m, the counter-rotary bottom circulation cell disappears but the temporal variation of the thickness of the bottom

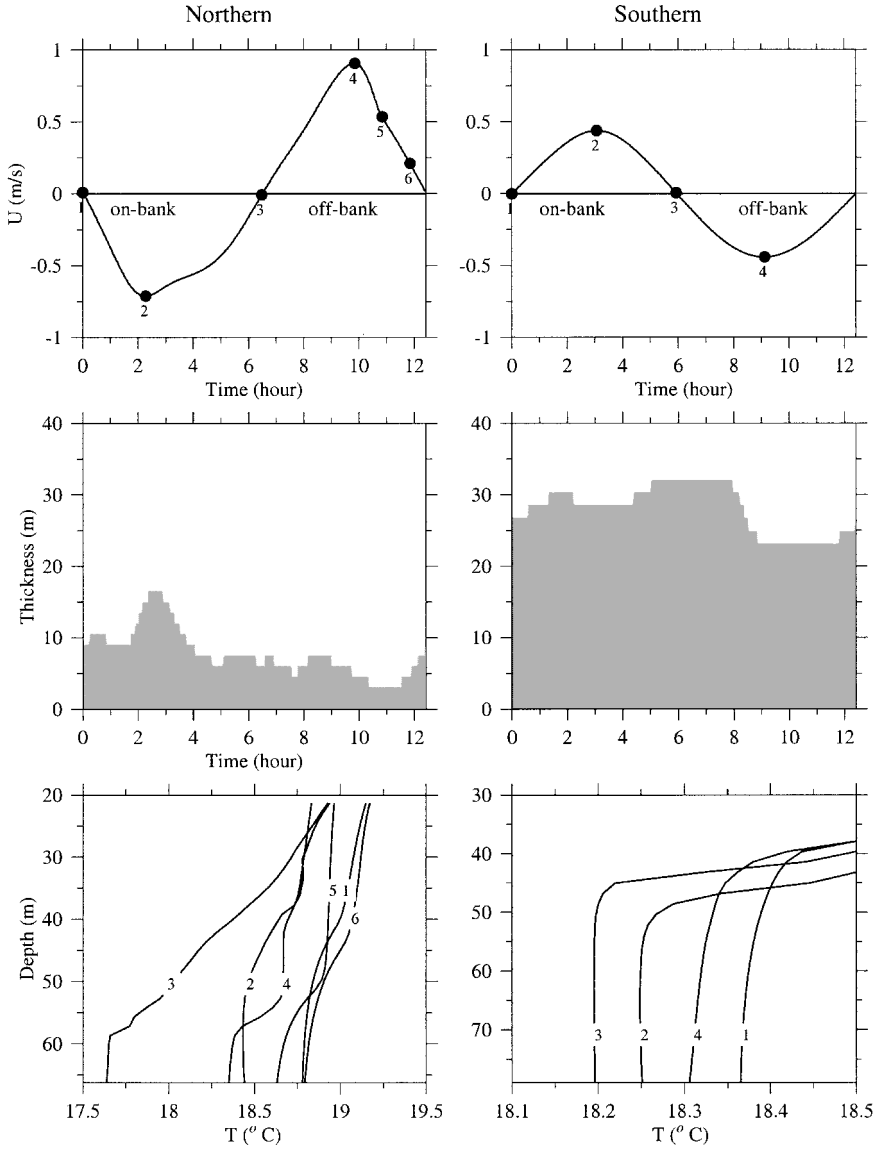

Figure 7. Time series of surface cross-bank current (top), height of the bottom mixed layer (middle), and vertical profile of temperature (bottom) over a tidal cycle at sites A and C on southern (right) and northern (left) flanks.

boundary layer is similar to that over the deeper slope. At site A, the height of the bottom boundary layer increases to a maximum of about 30 m during on-bank tidal flow and decreases to a minimum of about 23 m during off-bank tidal flow, with a co-range of about 7 m over a tidal cycle (Fig. 7).

On the steep northern flank, however, the off-bank current acts like a waterfall to advect warmer water downslope with a displacement of 50 m in a narrow region near the bottom (Fig. 6). As a result, a large cross-isobath temperature gradient forms over the slope. When the tidal flow reverses, the upslope current carries colder water upward along the slope, which decreases the cross-isobath temperature gradient within the bottom boundary layer. A deep depression of streamlines is found about 15 km away from the northern edge of the bank at maximum off-bank current. This structure also is observed at maximum on-bank current, but the depth of the depression is less and its width is wider. At site C, the height of the bottom boundary layer reaches a maximum of 15 m near maximum on-bank tidal current and decreases to a minimum of 3 m just after maximum off-bank current. The bottom mixed layer is poorly defined in four hours around the transition time from off-bank to on-bank flows due to strong mixing throughout the water column (Figs. 5 and 7). The bottom mixed layer reappears as the on-bank flow increases and mixing is restricted to the bottom.

Over the southern flank, the bottom boundary layer is characterized by a small gradient Richardson number ($R_i < 0.2$) over a tidal cycle. At site A, a negative R_i occurs at maximum on-bank current, with the maximum absolute value at about 8 m above the bottom (Fig. 8a), indicative of the unstable density gradient occurring during on-bank flow. Over the northern flank, the vertical structure of R_i is more complex. At site C, $R_i < 0.2$ occurs up to a height of 40 m above the bottom during the transition from off- to on-bank flow, consistent with the large mixing within the water column (Fig. 5). As over the southern flank, the near-bottom density gradient becomes unstable during on-bank flow, causing negative R_i.

d. Dissipation rate

Temporal and vertical variations of the turbulent dissipation rate ε at southern flank, top, and northern flank sites are shown in Figure 9. At site A, ε varies periodically with the cross-bank tidal current, reaching maximum values near the maximum cross-bank current. ε is largest near the bottom and decreases monotonically upward within the bottom boundary layer (Fig. 9a). ε is about 0.5×10^{-5} W/kg near the bottom at maximum on- and off-bank flows, and about 10^{-7} W/kg at the top of the bottom boundary layer. The time lag between the occurrence of maximum ε at the bottom and top of the boundary layer (thickness $\sim$40 m) is about 1 hour. This time lag is probably caused by the phase-lagged local production of turbulent kinetic energy (Simpson *et al.,* 1996).

At site B, ε also varies periodically with cross-bank tidal current, with a monotonic vertical decay (Fig. 9b). The maximum value of $\varepsilon \approx 8 \times 10^{-5}$ W/kg occurs at the bottom during maximum cross-bank flow. The vertical phase shift is still noticeable in Figure 9b but the time lag at the bottom and surface is less than 0.5 hour, suggesting a quicker upward transfer rate of the turbulent shear production. A similar time-dependent distribution of ε was found at a mixed site on the northeast flank of Georges Bank by Naimie (1996) in a

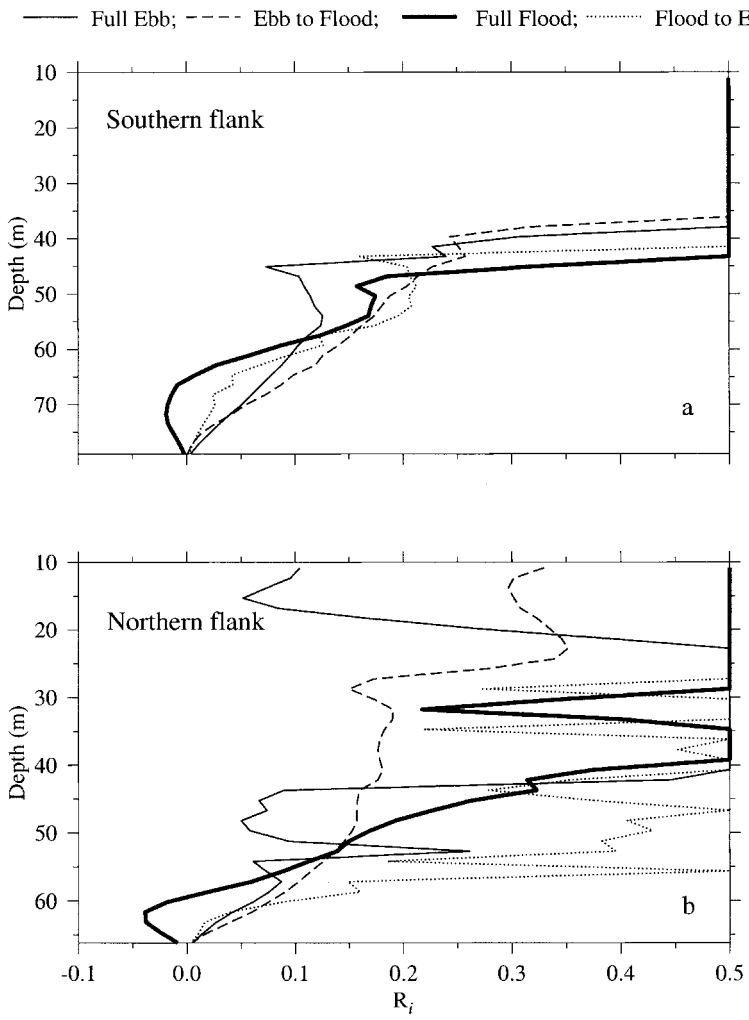

Figure 8. Vertical distribution of the gradient Richardson number (R_i) at full ebb, ebb to flood, full flood, and flood to ebb tides at sites A and C on southern (upper) and northern (lower) flanks.

3-D prognostic modeling experiment over Georges Bank [see Fig. 14 in Horne *et al.* (1996)].

The temporal and spatial variations of ε are much more complex at site C on the northern flank (Fig. 9c). In the bottom 10 m, ε is still characterized by two near-bottom maxima during one tidal cycle. The maximum value $\varepsilon \approx 1.0 \times 10^{-5}$ W/kg occurs near maximum on- and off-bank flows. Large values of ε are found throughout the water column around the transition between off- and on-bank flows. The maximum value of ε in that period varies from 0.5×10^{-5} W/kg near the bottom to 1.0×10^{-7} W/kg near the surface.

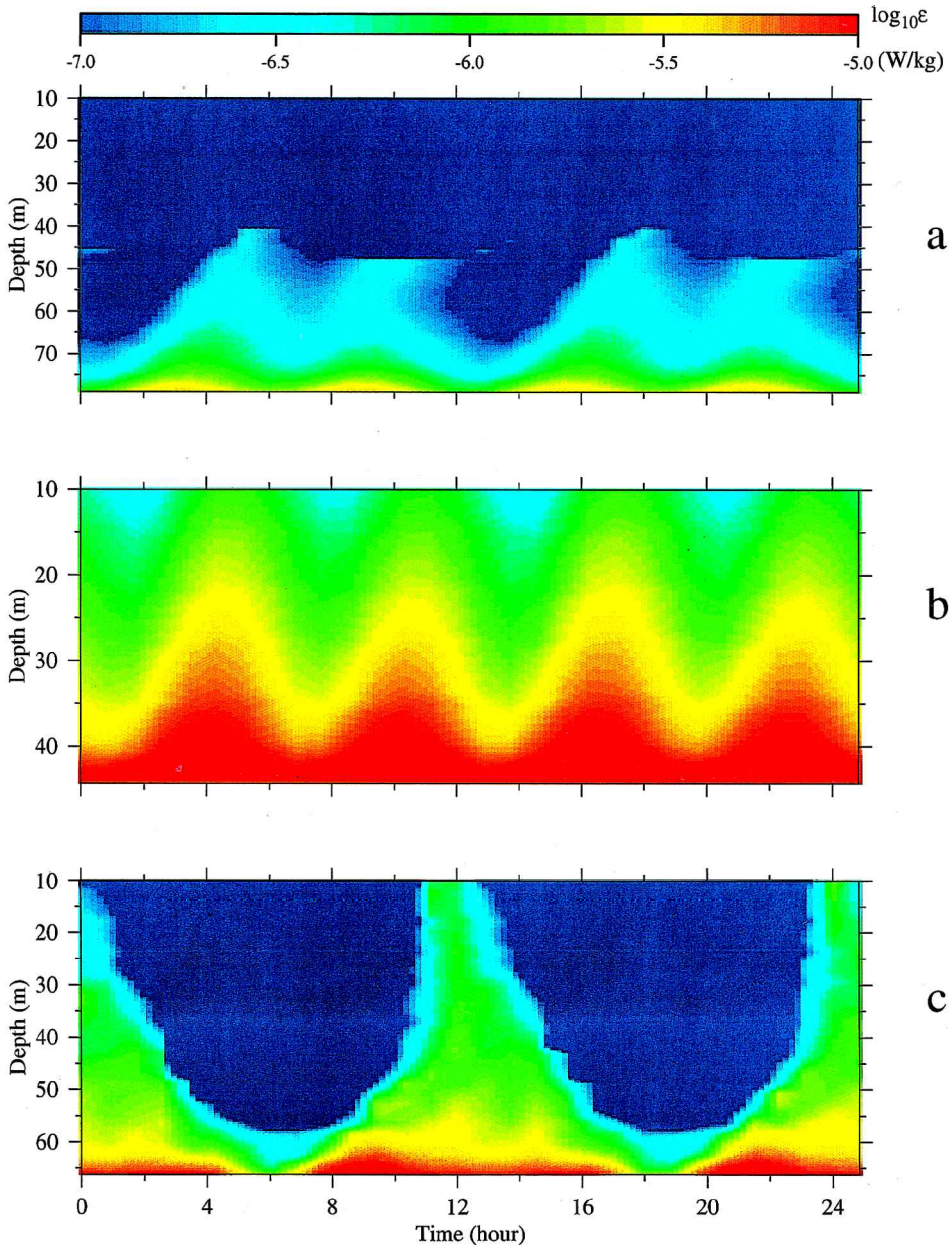

Figure 9. Time series of turbulent dissipation rates at site A, B, and C on the southern (a), crest (b), and northern (c) flanks over two tidal cycles.

These model-predicted values of ε can be compared with recent estimates based on *in-situ* microstructure measurements on Georges Bank. Burgett (1997) used power spectra of the observed velocity shear to estimate ε at the mixed site F and the stratified site E on the southern flank (Fig. 1). At the mixed site, ε varied periodically, having a large value near maximum off- and on-bank currents. The maximum ε was about 1.0×10^{-5} W/kg at the bottom and decreased to 1.0×10^{-6} W/kg at 35 m above the bottom. The vertical phase lag of maximum ε was less than one hour over the 45-m water column. At the deeper stratified site, the maximum ε was about 0.5×10^{-5} W/kg near the bottom and decreased to 1.0×10^{-7} W/kg at the base of the pycnocline, about 40 m above the bottom. The phase lag of maximum ε at the bottom and the base of the pycnocline was about two to two and a half hours. At site D on the northern flank, Yoshida and Oakey (1996) also found that ε varied periodically with on- and off-bank tidal flows, which reached a maximum value as ε exceeded 1.0×10^{-6} W/kg near the bottom and decreased to 1.0×10^{-7} W/kg at the base of the pcynocline, about 40 m above the bottom. Horne *et al.* (1996) found similar results at the mixed site H, where the maximum ε ranged from 1.0×10^{-5} W/kg at the bottom to $1.0 \times 10^{-6} - 0.5 \times 10^{-5}$ W/kg at a depth of 10 m below the surface.

A direct comparison between model and observed dissipation rates on the southern flank is shown in Figure 10. The observed data used in this comparison were obtained at an anchor station at site F, at the 45-m isobath on the southern flank, where the amplitude of cross-bank tidal current was about 70 cm/s. This site was about 40 km away from the cross-bank slice used in our model (Fig. 1). The model ε shown here was taken at a grid point at the 54-m isobath on the model southern flank where the cross-bank tidal current has the same amplitude as that observed at site F. The comparison is made at the times when the amplitudes of the tidal flow is 70 cm/s (Fig. 10a) and of 42 cm/s (Fig. 10b). The observed dissipation rates were calculated as a 10-sample average over one hour. Considering the uncertainty of measurements and the idealized 2D nature of the numerical model, the model dissipation rate agrees well in both magnitude and vertical phase with the observed ε within the water column. The disagreement near the surface is not surprising, since the large dissipation rate observed near the surface was caused by wind mixing which is not included in our current model study.

e. Balance of turbulent kinetic energy

The turbulent kinetic energy balance produced by the MY level 2.5 turbulent closure model for summer stratification is presented next. The results show that in the turbulent kinetic energy equation (1), the shear production of turbulence, P_s, approximately balances the turbulent dissipation ε over the bank (Fig. 11). For example, at 13.3 m above the bottom at site A, the nonlinear advection $[u(q^2)_x + w(q^2)_z]$ and vertical diffusion $[(K_q(q^2)_z)_z]$ terms are much smaller than $2P_s$ or 2ε, so that they can be neglected in the bottom boundary layer. Although the buoyancy production of turbulence term P_b is about one order of magnitude smaller than P_s, it plays an important role in mixing asymmetry during the on- and off-bank flows. The local change of turbulent kinetic energy $(q^2)_t$ is controlled by the approximate

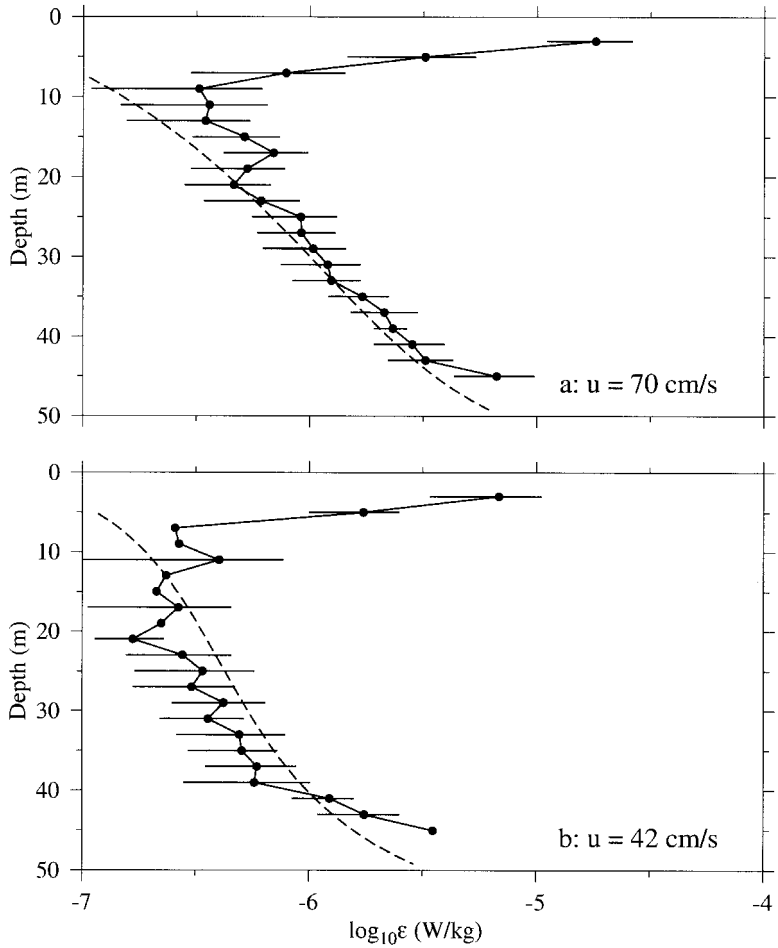

Figure 10. The comparison between model (dashed line) and observed turbulent dissipation rates at the times that the amplitude of the hourly-averaged, cross-bank tidal current was (a) 70 cm/s (a) and (b) 42 cm/s. The *in-situ* dissipation rate estimates were provided by D. Hebert, N. Oakey, and R. Burgett.

balance $2(P_s + P_b - \varepsilon)$. At site B, at 16.7 m above the bottom, P_b vanishes due to vertical mixing, and $u(q^2)_x + w(q^2)_z$ and $(K_q(q^2)_z)_z$ also are insignificant. The local change of turbulent kinetic energy $(q^2)_t$ is controlled by the difference between shear production and dissipation $2(P_s - \varepsilon)$. At site C, at 4.8 m above the bottom, the $u(q^2)_x + w(q^2)_z$, $(K_q(q^2)_z)_z$ and $2P_b$ are generally at least one order of magnitude smaller than $2P_s$ or 2ε except during a two-hour interval after maximum off-bank current when these terms contribute significantly to the turbulent energy balance over the northern flank. The tidally-averaged turbulent kinetic energy equation (Fig. 12) exhibits a similar approximate balance between

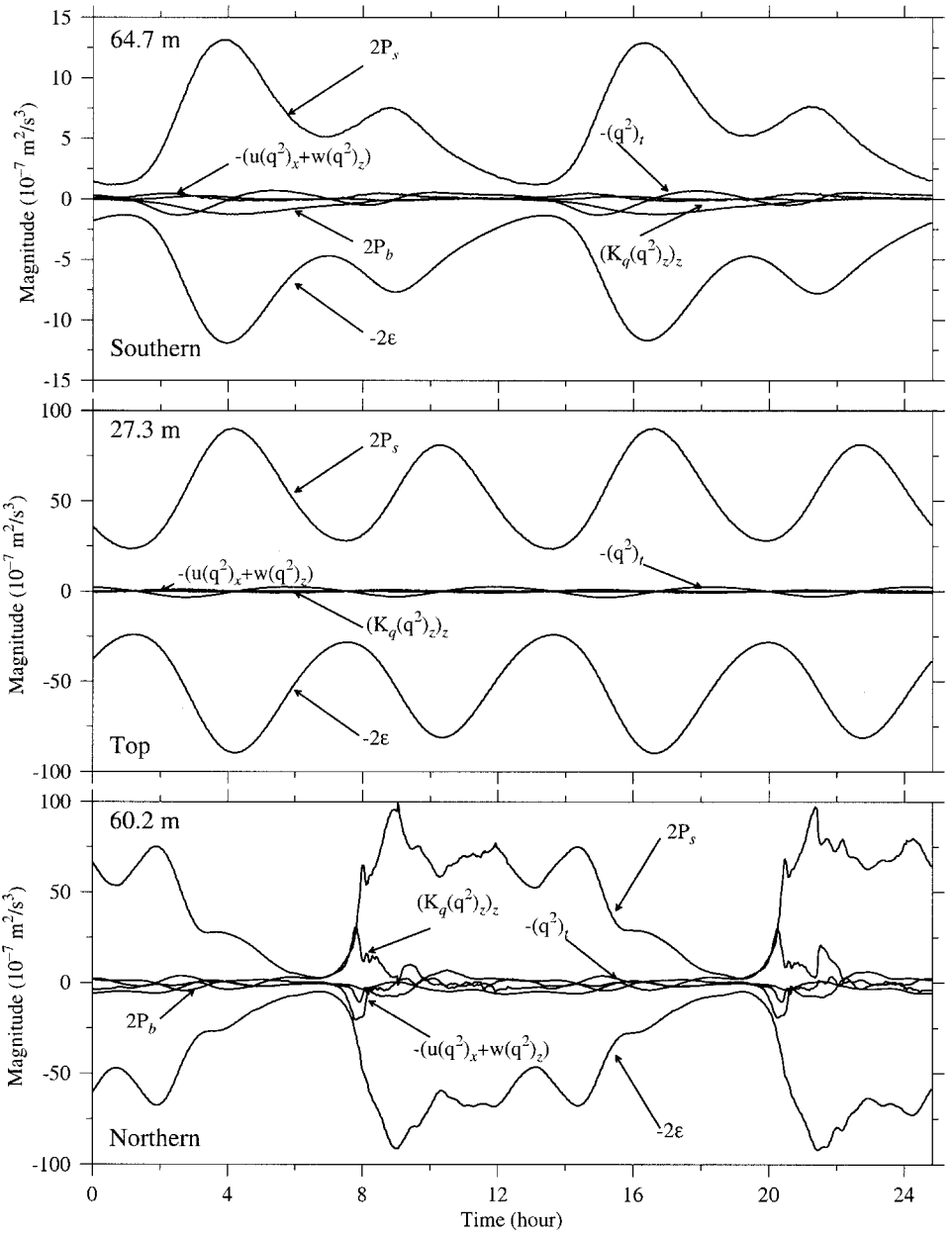

Figure 11. Time series of terms in the turbulent kinetic energy equation at depths of 64.7 m (13.3 m above the bottom) at site A (southern flank), 27.3 m (16.7 m above the bottom) at site B (crest), and 60.2 m (4.8 m above the bottom) at site C (northern flank).

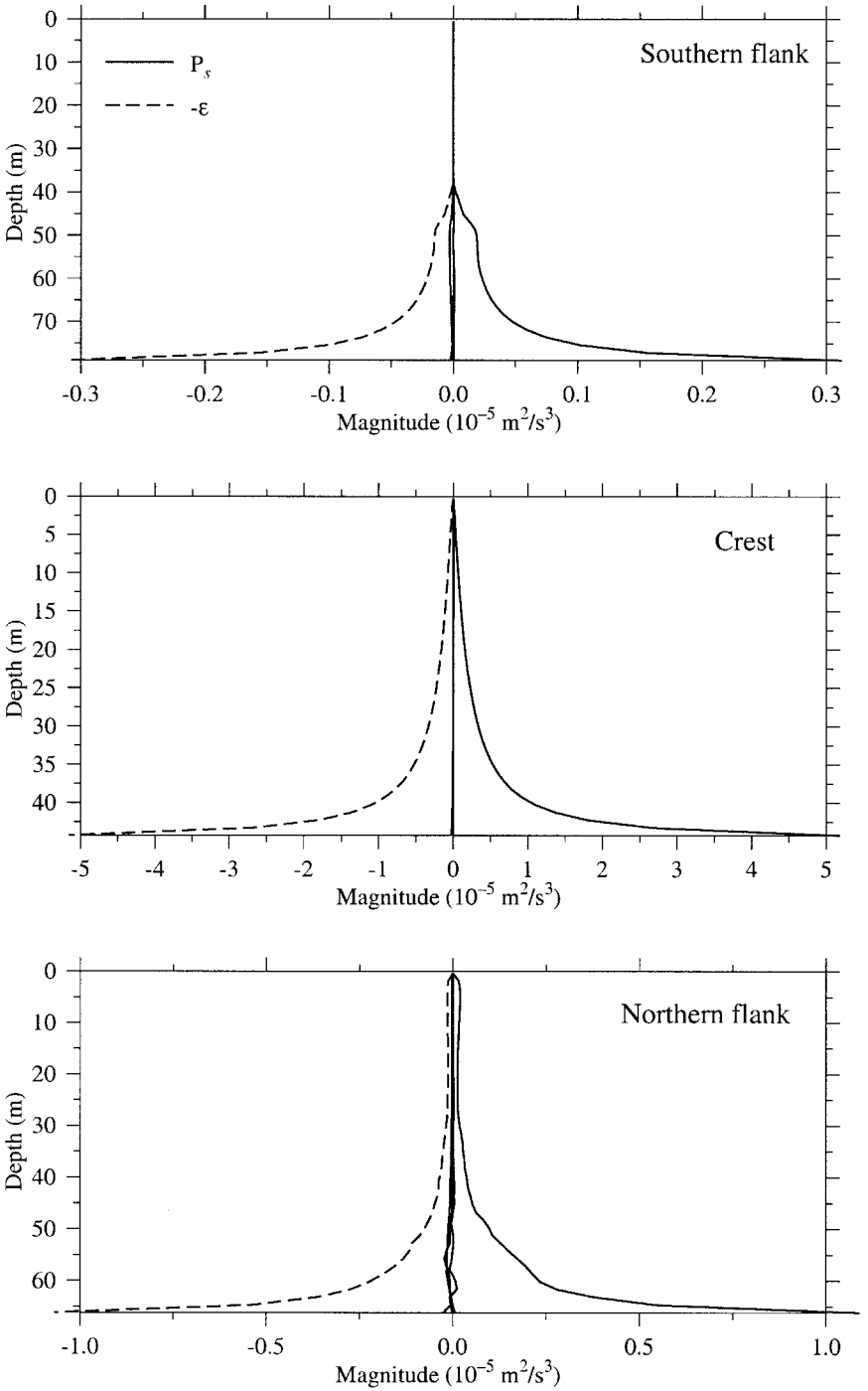

Figure 12. Vertical distribution of major terms in the turbulent kinetic energy equation at site A (southern flank), site B (crest), and site C (northern flank). All terms are averaged over a tidal cycle on the 15th model day.

shear production and dissipation, with both P_s and ε decaying vertically from maximum values at the bottom.

These model results suggest that tidal mixing over Georges Bank is driven primarily by local turbulent production, with a basic balance between shear production and dissipation. Although buoyancy production is generally much smaller than shear production, P_b contributes to mixing asymmetry during on- and off-bank flows. Over the southern flank and shallow top, tidal mixing is characterized by a vertical 1-D balance between shear production, buoyancy production (in the stratified region), and dissipation. On the northern flank where the bottom slope is large, as a first-order approximation, advection and vertical diffusion of turbulent kinetic energy also contribute to the turbulent kinetic energy balance.

4. Tide-induced internal waves

With sufficiently high vertical and horizontal resolutions, internal waves form at the edges of the model bank. Characteristics of these waves differ over the flanks. On the southern flank, the 19°C isotherm develops a small initial depression over the shelf break during maximum off-bank current (Fig. 13). This internal feature, approximately stationary during the period of decreasing off-bank flow, begins to move on-bank with a speed that varies over time. The fastest speed $c_o \approx 103$ cm/s occurs during a three-hour period bracketing the maximum on-bank current (time = 7 to 11 in Fig. 11). During that period, the time-averaged, on-bank current over the propagation region is $\overline{u} = 20$ cm/s. The local phase speed $c_p = c_o - \overline{u} \approx 83$ cm/s. This phase speed is in the range of 43 to 195 cm/s estimated for the lowest internal wave mode based on the mean density (temperature) profile and local water depth near site A (C&B).

The amplitude of this internal wave can be estimated from the vertical excursion of the 19°C isotherm. It decays in time as the water becomes shallower and disappears completely in the TMF (located near $x = 45$ km from the southern edge of the bank, Fig. 2). The maximum amplitude is about 8 m, occurring near $x = 5$ km at maximum on-bank current. The horizontal separation scale is about 15 km. The remarkable vertical variation of the temperature, which was found at site A near maximum on-bank current (Fig. 3), is a part of this internal wave feature at a location of the trough.

On the northern flank, a depression of the 19°C isotherm occurs at the outer edge of the bank one hour before the on-bank flow reverses (Fig. 14). This depression becomes sharper in the early phase of off-bank flow and then spreads horizontally as the TMF migrates off-bank. A second depression of the 19°C isotherm forms at the outer edge of the bank around maximum off-bank current. The maximum vertical scale of this thermal depression is about 50 m, occurring one hour after maximum off-bank flow. The amplitudes of these depressions decrease rapidly as they are advected onto the bank during on-bank tidal flow.

The formation of the depression at the northern edge of the bank might be a result of hydraulic jump that occurs on the lee side of the bank where the tidal motion becomes supercritical. At the 80-m isobath where the sharp depression begins during maximum off-bank flow, the vertically-averaged tidal current $\overline{u}_b$ is about 43 cm/s, very close to $c_o =$

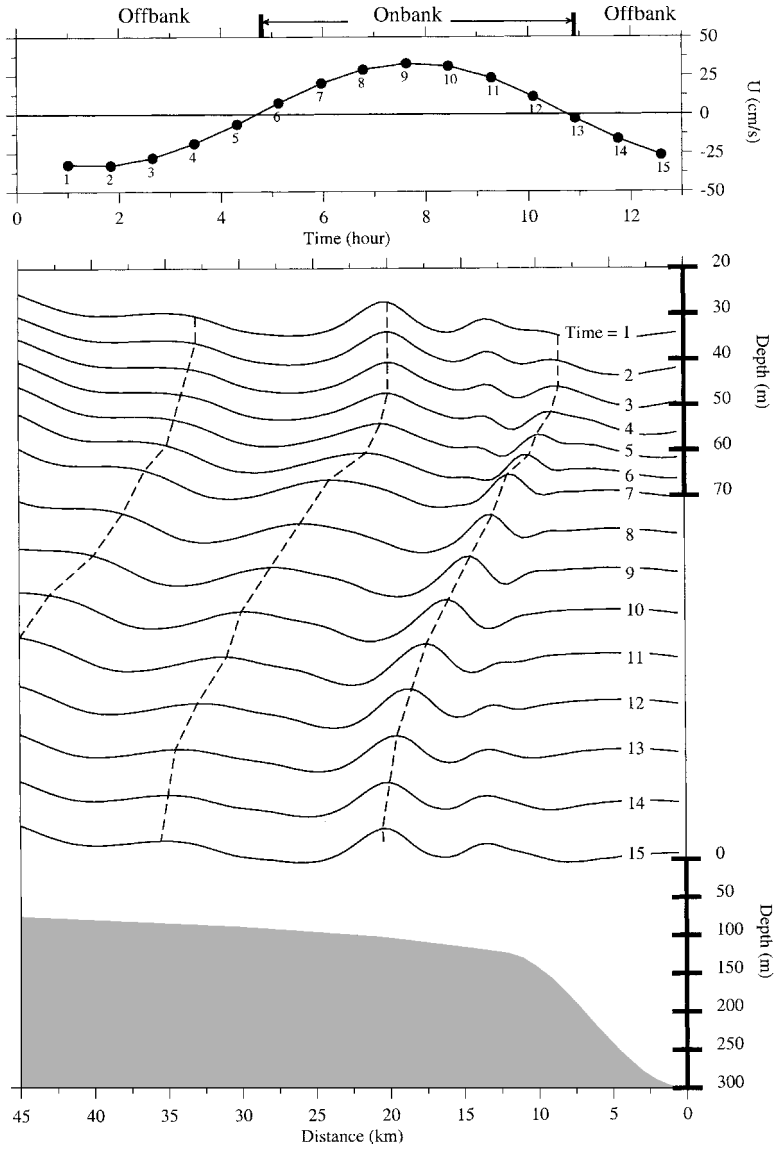

Figure 13. Time sequences of the cross-bank current (u) at the depth of 30 m on the 70-m isobath and the 19°C isothermal line on the southern flank over a tidal cycle. The isothermal line at time n is offset in the vertical by $10(n - 1)$ where n varies from 1 to 16. The mean depth of the 19°C isotherm at the 70-m isobath is about 35 m.

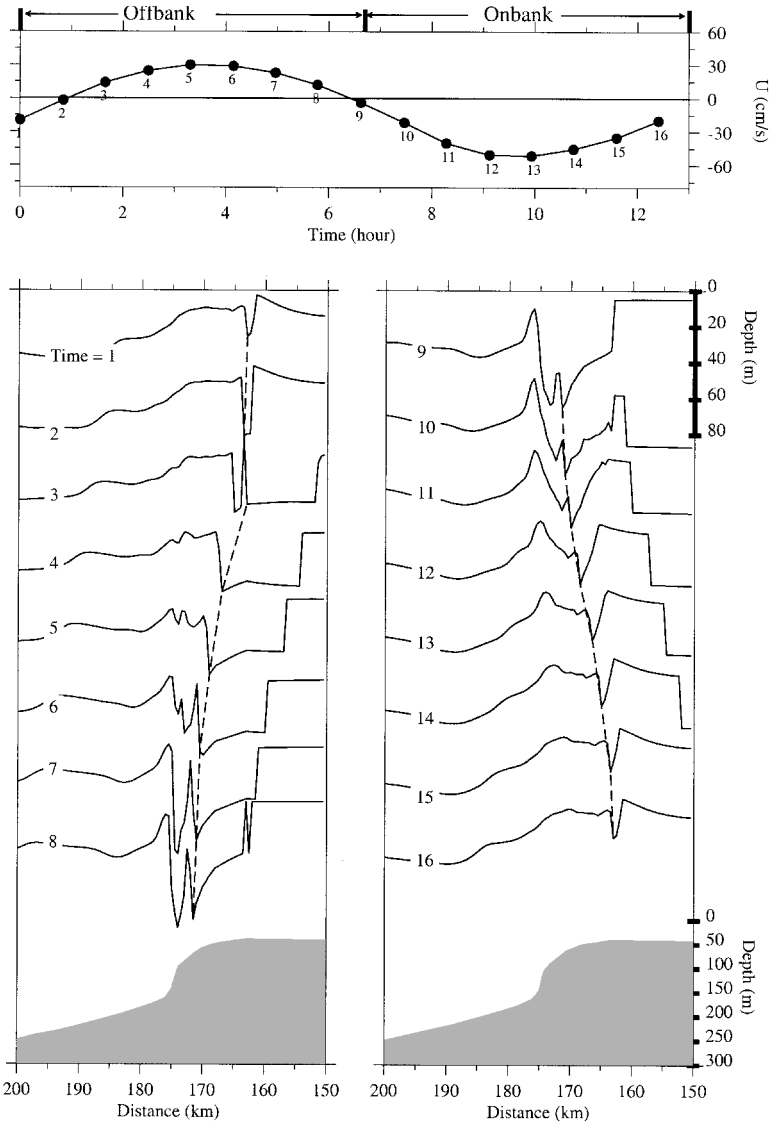

Figure 14. Time sequences of the cross-bank current (u) at the depth of 30 m on the 80-m isobath and the 19°C isothermal line on the northern flank over a tidal cycle. The isothermal line is offset in the vertical by $40(n-1)$ for $1 \le n \le 8$ and by $40(n-9)$ for $9 \le n \le 16$. The mean depth of the 19°C isotherm at the 80-m isobath is about 30 m.

45 cm/s, the propagation speed of the 19°C isotherm. At this time, the local wave phase speed $c_p = c_o - \overline{u}_b \approx 2$ cm/s (essentially zero), causing an accumulation of wave energy there (hydraulic jump). During maximum on-bank flow, $\overline{u}_b = 76$ cm/s and $c_o = 68$ cm/s, so that $c_p = c_o - \overline{u}_b \approx -8$ cm/s. This suggests that the wave is still propagating offshore while

it is being advected back onto the bank. The formation of the depression can be explained also by mass conservation. During off-bank flow, the steep bottom topography on the northern flank causes the current to converge near the surface at the edge of the bank. The maximum convergence occurs at maximum off-bank flow, causing a strong downward current and thus leading to the sharp depression of isotherms. The strong vertical shears associated with this depression contribute directly to strong tidal mixing found in the upper 50 m after maximum off-bank flow (Fig. 5).

5. Cross-bank water exchange

To study the cross-bank water exchange during tidal mixing and rectification, we released passive particles at different depths on both flanks of the model bank. Since the model tidal forcing increased from zero to full value over two tidal cycles, all particles were deployed at the time when the model forcing was at full strength and tidal mixing was just beginning at the end of the second tidal period. The primary experiments were conducted with summer stratification. Particle tracking was carried out for four weeks. In Figures 15 and 16, we show particle trajectories obtained after about 10.3 model days when an equilibrium state of tidal mixing is reached. In Figure 17, the particles are traced from their initial deployment positions. An alternative experiment in which particles were deployed at the end of the 10th model day were made to examine the sensitivity of particle trajectories to their initial locations; no significant differences were found for the pattern of particle trajectories over the bank. To investigate the effects of stratification on cross-bank transport, we also conducted experiments using weaker initial stratification and no stratification. In the weak stratification case, the initial temperature distribution was specified as a linear function of z, with a temperature of 13°C at the surface and 11°C at the bottom (Chen *et al.,* 1995).

a. Cross-frontal particle exchange

For the summer stratification case, particles released initially in the stratified region in the bottom boundary layer within the southern frontal zone mainly move in a clockwise residual circulation cell (Fig. 15) in addition to oscillating within a tidal excursion length of $2U/\omega$. Some particles near the bottom, however, move on-bank across the TMF with maximum speeds of 0.6–1.0 cm/s and enter the mixed region on the top of the bank. This suggests that a net on-bank water flux through the TMF can occur near the bottom on the southern flank. The clockwise pattern of residual particle trajectories is similar to the cross-bank secondary circulation pattern found by Garrett and Loder (1981), suggesting that ageostrophic frontal circulation is a predominant factor to the cross-bank flow on the southern flank.

At the northern edge, particles tend to be advected upslope along the sloping bottom and

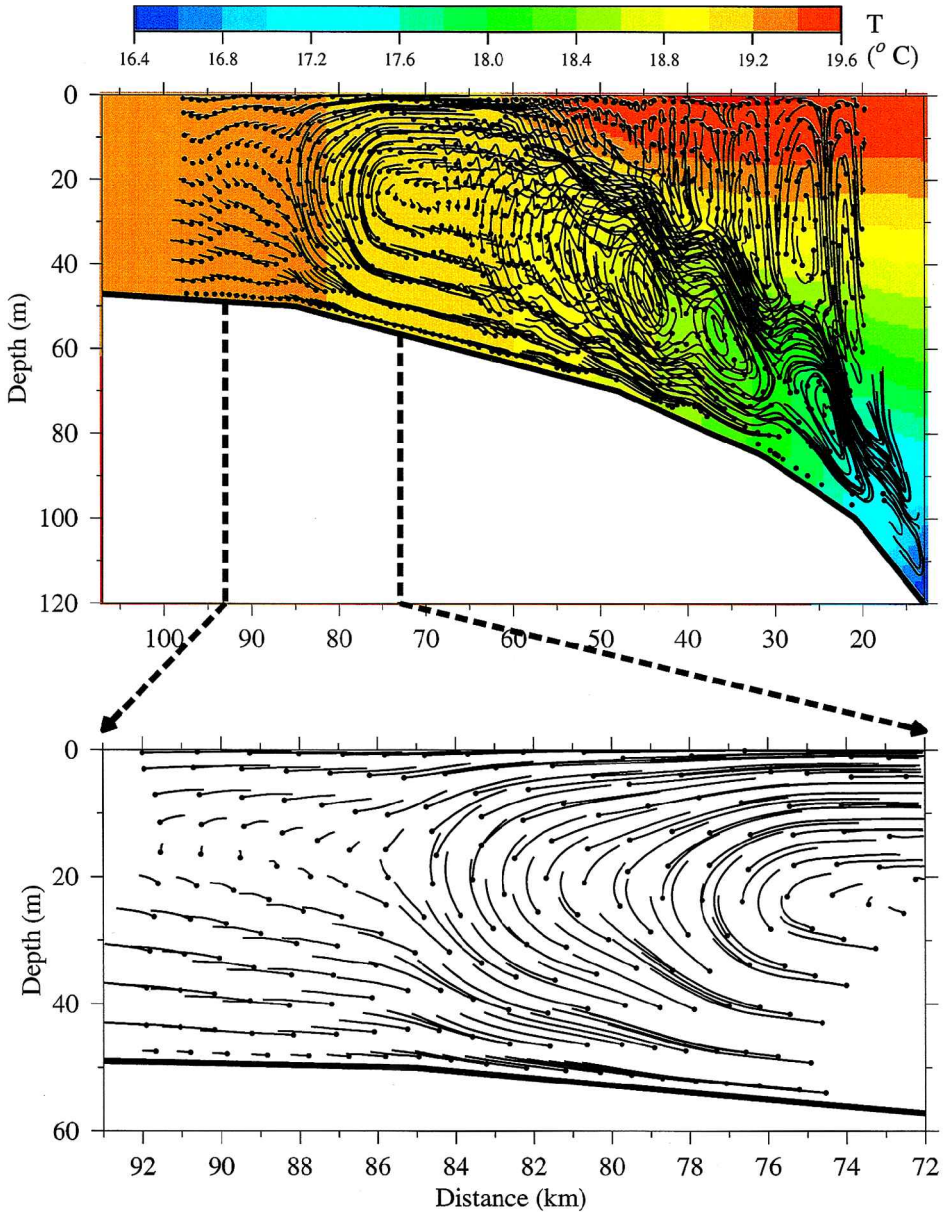

Figure 15. Tidal-cycle residual trajectories of particles on the southern flank for 19.67 days. The solid circle indicates the particle's location at which it started to be traced (after 10.3 model days).

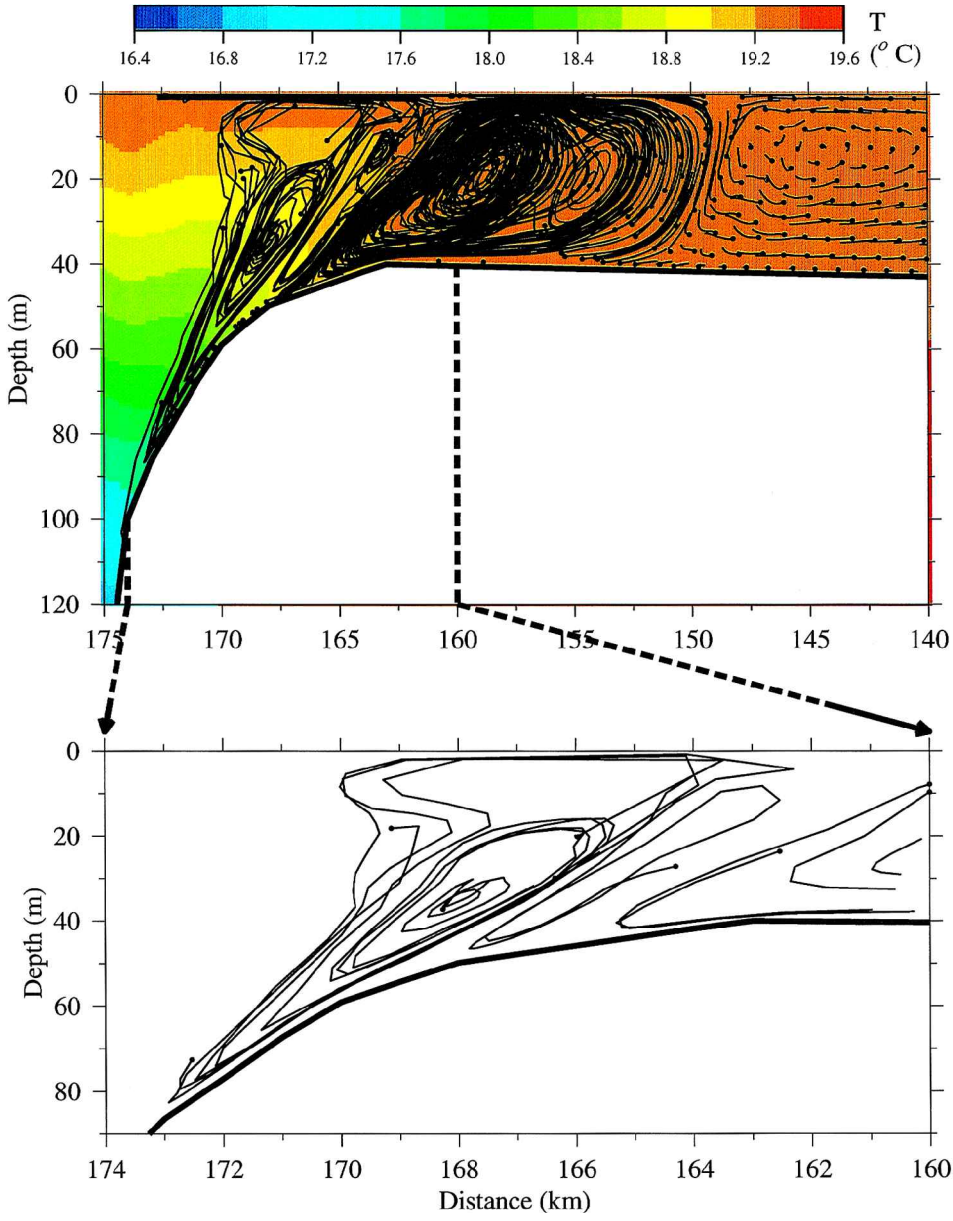

Figure 16. Tidal-cycle residual trajectories of particles on the northern flank for 19.67 days. The solid circle indicates the particle's location at which it started to be traced (after 10.3 model days).

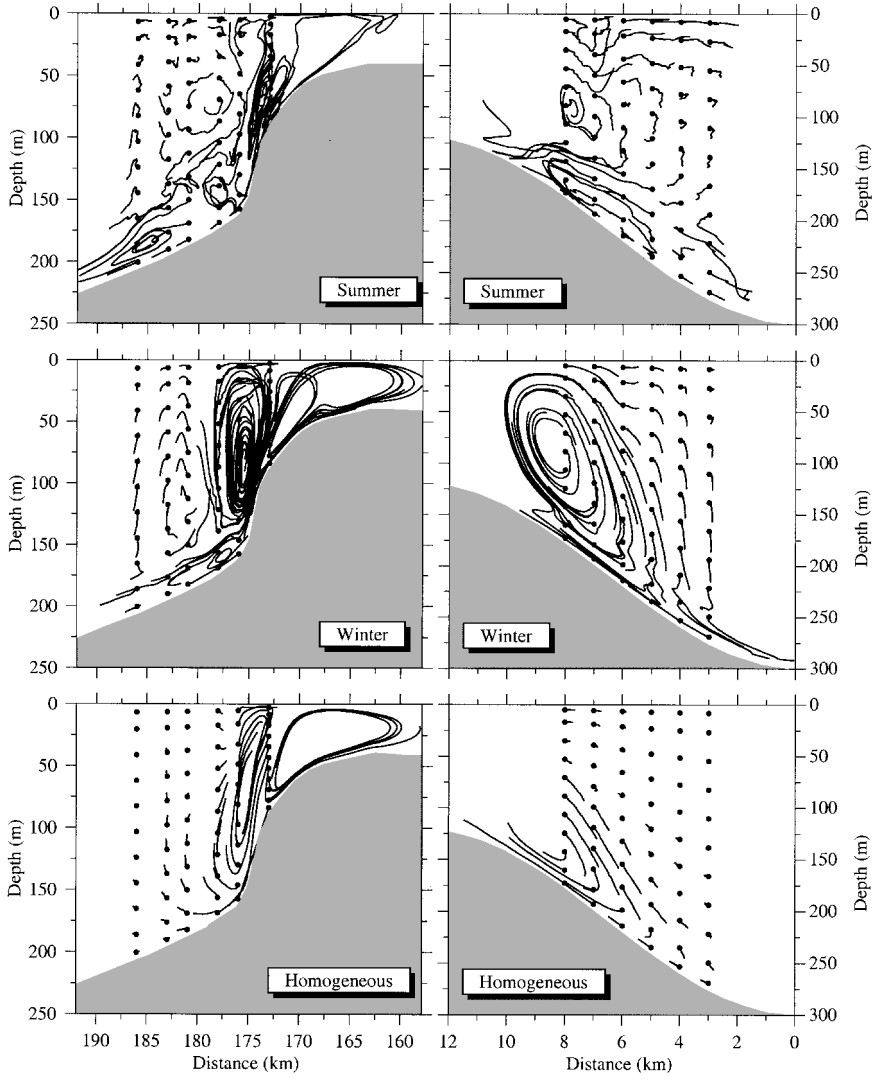

Figure 17. Tidal-cycle residual trajectories of particles on southern (right) and northern (left) slopes of the bank for summer (top), winter (middle), and homogeneous (bottom) cases. The solid circle indicates the particle's initial location (at the end of the second model day). The total track time is 28.98 days.

then recirculate counter-clockwise near the TMF (Fig. 16). Although many particles cross the front and enter the mixed region, they all tend to move back to the stratified region via gyres. The center of the counter-clockwise gyre is located about 5 km on-bank from the northern front. No particles leave this circulation cell except near the bottom where a few particles move onto the top of the bank.

b. Particle trajectories over the flanks

On the deep southern flank, particles released initially in the stratified region outside the sloping bottom boundary layer for the summer stratification move in a clockwise residual circulation cell. Particle trajectories near the bottom consist of two groups. Particles over the shallow slope (depth less than 250 m) tend to move upslope onto the bank, while particles over the deeper slope move offbank along the bottom (Fig. 17). The maximum mean up-slope speed is about 0.2–0.3 cm/s, occurring near the top of the bottom boundary layer. On the deep northern flank, the near-bottom particles below 180 m move downslope, though particles in the upper slope tend to climb along the sloping bottom. The up-slope velocity near the bottom in the upper slope is about 2 cm/s. At this speed, a particle at a depth of 74 m could be carried to the surface along the slope in about 4 days.

Particle trajectories in the weak stratification case are very different from those in the summer stratification case. On the southern slope, although the pattern of the trajectories is similar to that found in the summer stratification case, particle trajectories in the shallow slope above 250 m are characterized by a much stronger clockwise gyre with a center at the depth of 75 m on the 150-m isobath. The particles near the bottom in the deep slope also move off-bank at a much faster speed. On the northern slope, particles near the bottom in the upper slope (shallower than 100 m) generally move in a counter-clockwise cell, with an upslope flow near the bottom. Particles in the deep slope tend to move along two paths, one in a narrow, elliptically clockwise cell, and another off-bank along the bottom.

Trajectories of particles in the homogeneous case are very similar to those in the weak stratification case: a single clockwise Lagrangian residual circulation cell on the southern slope and double Lagrangian circulation cells on the northern slope. However, on the southern slope, the mean particle displacements are almost zero in the upper layer, so that the residual movement of particles is restricted to the bottom. This is consistent with the theory of barotropic tidal rectification. That theory suggests that the tidal residual flow is significant only over a sloping bottom where nonlinear advection and friction are large (Loder, 1980; Zimmerman, 1978; C&B). The same applies to the northern slope, where mean particle motion is restricted in the narrow region over the steep bottom topography and the mean particle displacements in the deep off-bank region tend to be zero (Fig. 17).

c. The Euler-Lagrange comparison

The particle trajectories described above differ from the patterns of cross-bank residual Eulerian circulation shown in Figure 2. On the southern flank, the residual Eulerian field has multiple closed circulation cells within the frontal zone between the 50- and 100-m isobaths, while particle trajectories show a clockwise cell at the front and more complex multiple cells within the frontal zone. According to the Lagrangian particle trajectories, water is upwelled at the edge of the front and moves to the stratified region near the surface. A convergence region exists near the surface in the stratified side, which pushes particles to move downward along the top of the bottom mixed layer. Some of these particles are

recirculated in multiple cells in the bottom mixed layer or the upper stratified region within the frontal zone.

On the northern flank, the Eulerian field features a clockwise residual circulation cell at the front with downwelling along the bottom (Fig. 2), while the Lagrangian particle trajectories suggest a counterclockwise residual circulation cell with upwelling along the bottom (Fig. 16). These two patterns are completely opposite! To check our model results, we repeated our experiment by releasing particles after the TMF reached an equilibrium state. The results of the particle trajectories were almost identical.

The trajectory of a selected particle is shown in Figure 18 to examine particle displacement over a tidal cycle on the northern flank. This particle was initially released at a depth of 82 m near the bottom after 15 model days. During the first tidal cycle, the particle moves over an excursion of about 80 m in the vertical and 5 km in the horizontal. After one tidal period, the position of the particle shifts about 1.2-km on-bank and 11.4 m upward. The tidally-averaged Lagrangian velocity of that particle was about -3 cm/s in the cross-bank direction (on-bank) and about 0.03 cm/s in the vertical (upward). The tidally-averaged, near-bottom Eulerian velocity at the 80-m isobath on the northern flank is about 9 cm/s in the cross-bank direction (off-bank) and -0.09 cm/s in the vertical (downward). This suggests that the tidally-averaged Stokes velocity is about -12 cm/s in the cross-bank direction (on-bank) and about 0.12 cm/s in the vertical (upward). Thus the particle follows a similar pattern in successive tidal cycles and moves up from a depth of 80 m to 25 m over 10 tidal cycles.

These experiments with Lagrangian particle tracking suggest that the residual Lagrangian and Eulerian currents are very different over Georges Bank. Strong nonlinearity on the northern flank can cause the cross-bank Lagrangian current to oppose the cross-bank Eulerian current over the upper slope at the edge of the bank. The different Eulerian and Lagrangian current patterns were suggested first by Loder and Wright (1985) based on the truncated Taylor series expansion and also were demonstrated in a particle-tracking model study for homogenous case by Loder *et al.* (1997). Opposite directions of cross-bank Eulerian and Lagrangian currents in a strong stratified case have not been demonstrated until this current study.

d. Passive tracer experiments

In the summer stratification case, the particle trajectories indicate an up-slope water transport on both southern and northern slopes of the bank. Cross-isobath flow is further examined here using a passive tracer. Experiments were made with two different initial distributions of a passive tracer

$$P = \begin{cases} 0 & \text{as} \quad z < 50\ \text{m} \\ 1 & \text{as} \quad z \geq 50\ \text{m} \end{cases} \quad \text{(case 1)} \qquad \text{and} \qquad P = \begin{cases} 0 & \text{as} \quad z < 150\ \text{m} \\ 1 & \text{as} \quad z \geq 150\ \text{m} \end{cases} \quad \text{(case 2)},$$

where P is the concentration of the tracer. To examine the influences of advection and diffusion on the movement of P, we have run the model with pure advection and advection

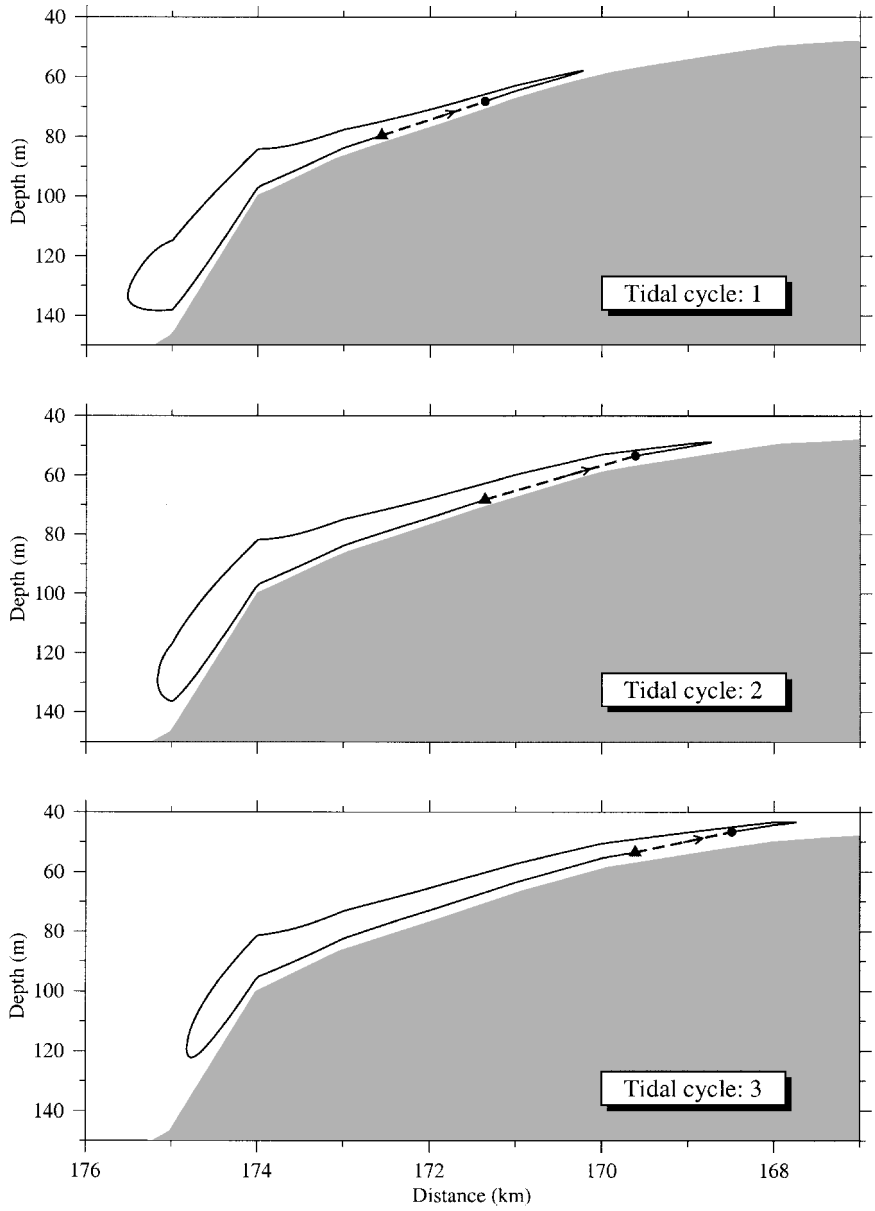

Figure 18. The trajectories of a particle over three tidal cycle on the northern flank. That particle was released at the beginning of the 15th model day. The filled triangle and circle indicate the starting and ending positions of the particle over each tidal period.

plus diffusion, respectively. For this study, we used the Multidimensional Positive Definite Advection Transport Algorithm (MPDATA) introduced by Smolarkiewicz (1984). The basic concept of this scheme is the successive application of an upwind scheme with a correction to the first-order truncation error by using a so-called "anti-diffusion" velocity. The repeated procedure yields a positive definite advection algorithm with second-order accuracy (Smolarkiewicz and Clark 1986; Smolarkiewicz and Grabowski, 1990).

Figure 19 shows the distribution of P at the initial time and the 10th day on the northern flank for case 1 and on the southern flank for case 2. With no diffusion ($K_c = 0$), the model exhibits an up-slope advection toward the TMF on both southern and northern flanks. The net up-slope advection of P is increased and spread out when tracer diffusion ($K_c \neq 0$) is added. These passive tracer experiments are consistent with the basic results of the particle tracking experiments described in the previous section, and support the suggestion that a tidally-induced physical mechanism can transport materials (e.g., nutrients) upslope on both sides of Georges Bank during summer.

6. Discussion

Past field work provides evidence of the up-slope intrusion of nutrient-rich slope water on the southern flank and nutrient-rich Gulf of Maine intermediate water on the northern flank during summer (Hopkins and Garfield 1979; Magnell *et al.,* 1981; Pastuszak *et al.,* 1982). The prevailing winds in summer are northeastward which tend to generate upwelling on the southern flank and downwelling on the northern flank. The fact that nutrients are advected over both flanks suggests that another physical mechanism besides wind forcing (which is weak in summer) must be important. The model particle trajectory and tracer experiments presented above suggest that upwelling can occur near the bottom in the shallow slope on both sides of the bank during strong summer stratification. The formation of these upwelling currents is associated with stratified tidal rectification over a sloping bottom topography.

The 2-D model results presented here are generally consistent with recent 3-D model experiments conducted by Naimie (1996) using more realistic Georges Bank/Gulf of Maine topography and climatological hydrographic conditions. Analysis of the turbulent kinetic equation in our study suggests that tidal mixing over Georges Bank is characterized to lowest order by a 1-D balance between shear production of turbulence, buoyancy production (in the stratified region), and turbulent dissipation. This result indicates that the 1-D MY-2.5 model used in the 3-D circulation model by Naimie (1996) is a good approximation for tidal mixing over most of Georges Bank except perhaps the northern flank where advection of turbulent kinetic energy can contribute to the local balance. The 1-D nature of turbulence with a basic balance between turbulent shear production and dissipation found over Georges Bank is consistent with the method that is widely used to estimate the turbulent dissipation rate from the field measurement data (Osborn, 1980). In that method, the dissipation rate is proportional to the variance of vertical shear of velocity.

Simpson *et al.* (1996) examined the vertical structure of turbulent dissipation at mixed

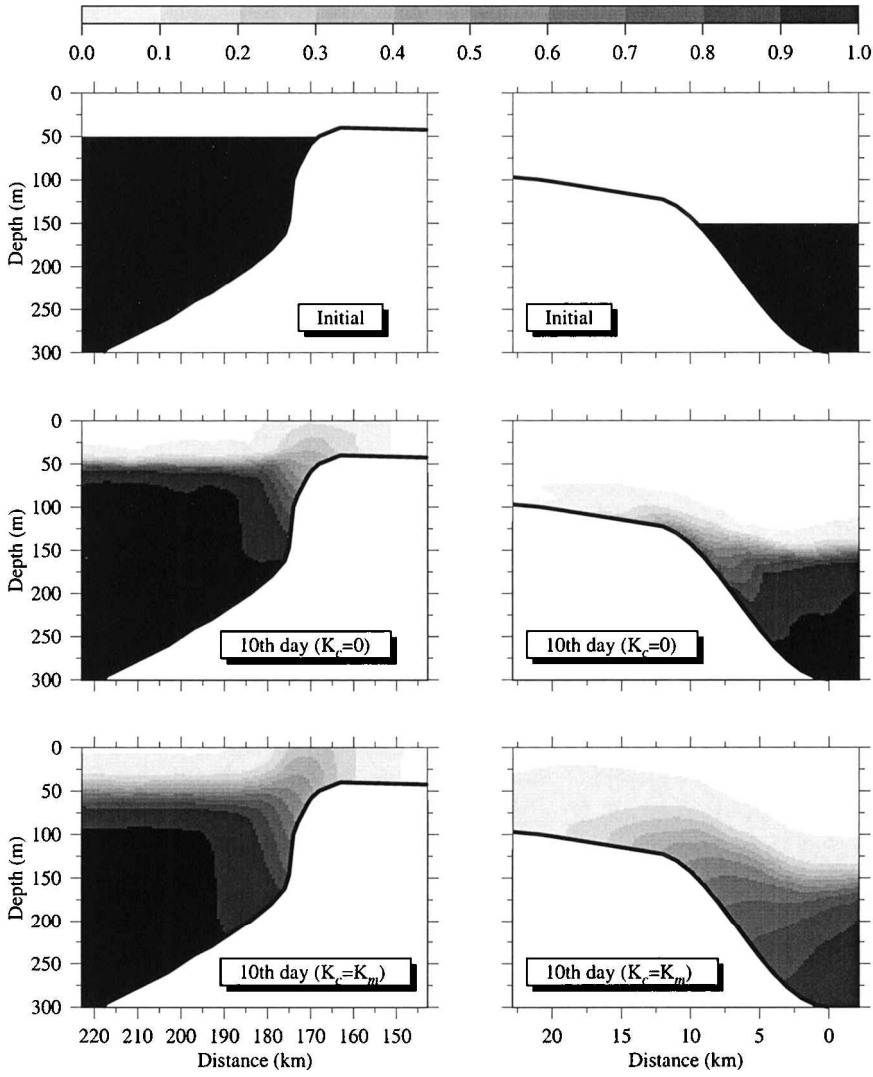

Figure 19. Distributions of passive tracer P at the initial time and at the end of the 10th computing day on the northern (left) and southern (right) flanks for the cases with pure advection and advection plus diffusion. The image of P at the 10th day is averaged over a tidal cycle.

and stratified sites in the Irish Sea by using the original version of the MY levels 2.0 and 2.2 turbulent closure models (Mellor and Yamada, 1974). They found that the dissipation rate, ε, exhibited a strong tidal variation with a pronounced phase lag in the vertical. A comparison of their model results with field data suggests that the MY level 2.2 model provides a better description of tidal mixing than the MY level 2.0 model. Our model results are consistent with their finding. Although the shear and buoyancy productions are

mainly balanced by dissipation in the MY 2.5 model, the vertical diffusion, as a first order approximation, may play a role in the transfer of turbulent kinetic energy upward from the bottom into the interior.

Our hydrostatic model with a high vertical resolution shows the formation of a hydraulic jump on the northern flank similar to that found by Lamb (1994) using an inviscid nonhydrostatic model. In his experiments, the initial depression evolves into large-amplitude solitary-like internal waves. This behavior is not seen in our experiments, due both to the hydrostatic vertical momentum balance and the inclusion of turbulent mixing.

7. Summary

High resolution numerical experiments over a 2-D asymmetric bank provide a detailed picture of tidal mixing, internal wave generation, and cross-bank particle exchanges. The model bathymetry represents a southeast-northwest slice across Georges Bank, with a broad southern flank, shallow crest, and steep northern flank. The model results show that tidal mixing varies in time and space over the bank. On the southern flank, the strongest tidal mixing occurs within the bottom boundary layer around the maximum on-bank tidal flow. This is caused by a gravitational instability near the bottom when denser water was advected upslope over lighter water. On the northern flank, the temporal variation of tidal mixing near the bottom is similar, except that strong turbulent mixing occurs throughout the upper 50 m of the water column associated with a deep thermal depression that forms after maximum off-bank tidal flow.

The model turbulent dissipation rate, ε, exhibits a strong tidal variation with a phase lag in the vertical. During a tidal cycle, ε is generally largest around the maximum on- and off-bank tidal flow. In the vertical, ε is generally larger near the bottom and decreases upward, with maximum ε occurring first near the bottom. At site A in the stratified region on the southern flank, the maximum ε is about 0.5×10^{-5} W/kg near the bottom and decays to about 10^{-7} W/kg at the top of the bottom mixed layer. The phase lag of the maximum ε between the bottom and top of the bottom layer ($\sim$40 m) is about one hour. At site B in the mixed region on the crest of the bank, ε varies from a near-bottom maximum of about 8×10^{-5} W/kg to about 10^{-6} W/kg at the height of 35 m above the bottom, with a vertical phase lag of less than 0.5 hour. At site C on the northern flank, the temporal and vertical variations of ε are much more complex. Within 10 m of the bottom, ε is still characterized by two maximum cores over one tidal cycle, with a maximum value of about 10^{-5} W/kg. Large dissipation is found throughout the water column after maximum off-bank flow, associated with the large thermal depression which forms during off-bank flow. The model-predicted dissipation profiles agree well with microstructure measurements made recently on the southern flank of Georges Bank during the US GLOBEC/Georges Bank program.

During stratified tidal rectification, fluid particles are advected up-slope near the bottom in the upper slope region (depth $<$150 m) on both northern and southern flanks of the bank. Particles also can move across the TMFs near the bottom. The Lagrangian trajectories of

particles differ significantly from those predicted by the residual Eulerian current field. On the northern flank, the near-bottom residual Lagrangian current is opposite in direction to the residual Eulerian current over the upper slope, suggesting that the Stokes velocity is comparable or larger than the residual Eulerian velocity due to the highly nonlinear nature of the flow there. The model up-slope mean advection of fluid particles is consistent with an alternative study of passive tracer evolution. With no diffusion, the tracer is carried up-slope near the bottom toward the TMF on both flanks of the bank. This up-slope tracer flux is increased when diffusion is added. Taken together, the model particle tracking and passive tracer results suggest that strong tidal forcing of a stratified fluid over the bank provides one physical mechanism responsible for high concentrations of nutrients and hence phytoplankton at the TMFs on Georges Bank.

This model study focuses on physical processes driven by strong tidal forcing of a stratified fluid over a finite-amplitude asymmetric bank in a highly idealized setting, with one objective being to develop better intuition about those processes which may dominate flow and stratification on Georges Bank. Additional model studies are now underway to examine the influences of surface forcing (both wind stress and heat flux) and more realistic 3-D topography and initial stratification on the tidally-forced flow over Georges Bank. Preliminary results suggest that the basic patterns of near-bottom tidal mixing, dissipation, and particle motion are similar to those described here. We hope to present the results of these new numerical experiments shortly in this sequence of idealized model studies.

Acknowledgments. This research was supported by the NSF/NOAA US GLOBEC Georges Bank Program under grants NA56RG0487 to Changsheng Chen and under NSF grant OCE93-13671 and OCE96-32357 to Robert Beardsley. The turbulent dissipation data used in this paper were provided by Dave Hebert (URI), Neil Oakey (BIO), and Russ Burgett (URI) under NSF grants OCE93-13671 and OCE96-31175. We want to express our thanks for their efforts in the analysis and interpretation of the data. The direct comparison between model-predicted and observed turbulent dissipation rates would be impossible without their kind and generous support. We also want to thank Glenn Flierl at MIT, Glen Gawarkiewicz, Karl Helfrich and Steve Lentz at WHOI for their valuable comments and suggestions. Two anonymous reviewers provided many critical comments and constructive suggestions which really helped to improve the model-data comparisons and clarify the final manuscript. This paper is U.S. GLOBEC contribution no. 107.

REFERENCES

Baines, P. G. 1982. On internal tide generation models. Deep-Sea Res., *29,* 307–338.

Blumberg, A. F. and G. L. Mellor. 1987. A description of a three-dimensional coastal ocean circulation model. Three-Dimensional Coastal Models. Amer. Geophys. Union, 1–16.

Brown, W. S. 1984. A comparison of Georges Bank, Gulf of Maine, and New England shelf tidal dynamics. J. Phys. Oceanogr., *14,* 145–167.

Burgett, R. 1997. The structure of tidal mixing on the southern flank of Georges Bank. M.S. thesis, University of Rhode Island, 142 pp.

Burgett, R., D. Hebert and N. Oakey. 1996. U.S. GLOBEC Georges Bank microstructure data. GSO Technical Report No. 96-6, 414 pp.

Chapman, D. C. 1985. Numerical treatment of cross-shelf open boundaries in a barotropic coastal model. J. Phys. Oceanogr., *15,* 1060–1075.

Chen, C. and R. C. Beardsley. 1995. A numerical study of stratified tidal rectification over finite-amplitude banks. Part I: Symmetric banks. J. Phys. Oceanogr., *25,* 2090–2110.

Chen, C., R. C. Beardsley and R. Limeburner. 1995. A numerical study of stratified tidal rectification over finite-amplitude banks. Part II: Georges Bank. J. Phys. Oceanogr., *25,* 2111–2128.

Chen, C., H. Tian, R. C. Beardsley and P. J. S. Franks. 1998. Influences of diurnal heat flux on circulation and stratification over Georges Bank and adjacent coastal regions: a 3-D prognostic modeling study. J. Geophys. Res., (submitted).

Farmer, D. M. and J. D. Smith. 1980. Tidal interaction of stratified fluid with a sill in Knight Inlet. Deep-Sea Res., *27A,* 239–254.

Flagg, C. N. 1987. Hydrographic structure and variability, *in* Georges Bank, R. H. Backus, ed., MIT Press, 108–124.

Galperin, B., L. H. Kantha, S. Hassid and A. Rosati. 1988. A quasi-equilibrium turbulent energy model for geophysical flows. J. Atmos. Sci., *45,* 55–62.

Garrett, C. J. R. and J. W. Loder. 1981. Dynamical aspects of shallow sea fronts. Phil. Trans. Roy. Soc. Lond., *A302,* 563–581.

Hopkins, T. S. and N. Garfield III. 1979. Gulf of Marine Intermediate Water. J. Mar. Res., *37,* 103–139.

Horne, E. P. W., J. W. Loder, C. E. Naimie and N. S. Oakey. 1996. Turbulence dissipation rates and nitrate supply in the upper water column on Georges Bank. Deep-Sea Res., *43,* 1683–1712.

Lamb, K. G. 1994. Numerical experiments of internal wave generation by strong tidal flow across a finite-amplitude bank edge. J. Geophys. Res., *99,* 843–864.

Lentz, S. J. and J. H. Trowbridge. 1991. The bottom boundary layer over the northern California shelf. J. Phys. Oceanogr., *21,* 1186–1201.

Loder, J. W. 1980. Topographic rectification of tidal currents on the sides of Georges Bank. J. Phys. Oceanogr., *10,* 1399–1416.

Loder, J. W., D. Brickman and E. P. W. Horne. 1992. Detailed structure of currents and hydrography on the northern side of Georges Bank. J. Geophys. Res., *97,* 14331–14351.

Loder, J. W. and E. P. W. Horne. 1991. Skew eddy fluxes as signatures of nonlinear tidal current interactions, with application to Georges Bank. Atmos.-Oceans., *29,* 517–546.

Loder, J. W., Y. Shen and H. Ridderinkhof. 1997. Characterization of three-dimensional Lagrangian circulation associated with tidal rectification over a submarine bank. J. Phys. Oceanogr., *27,* 1729–1742.

Loder, J. W. and D. G. Wright. 1985. Tidal rectification and front circulation on the sides of Georges Bank. J. Mar. Res., *43,* 581–604.

Longuet-Higgins, M. S. 1969. On the transport of mass by time-varying ocean currents. Deep-Sea Res., *16,* 431–447.

Magnell, B. A., J. J. Cura, C. N. Flagg and D. E. Frye. 1981. Interpretation of the physical oceanography of Georges Bank. Preliminary results. U.S. Department of the Interior, Bureau of Land Management, by EG&G Environmental Consultants, Contract AA 851-CTI-39, 186 pp.

Marsden, R. F. 1986. The internal tide on Georges Bank. J. Mar. Res., *44,* 35–50.

Matsuno, T., S. Kanari, C. Kobayashi and T. Hibiya. 1994. Vertical mixing in the bottom mixed layer near the continental shelf break in the East China Sea. J. Oceanogr., *50,* 437–448.

Maxworthy, T. 1979. A note on the internal solitary waves produced by tidal flow over a three-dimensional ridge. J. Geophys. Res., *33,* 338–346.

Mellor, G. L. and T. Yamada. 1974. A hierarchy of turbulence closure models for planetary boundary layers. J. Atmos. Sci., *33,* 1791–1896.

—— 1982. Development of a turbulence closure model for geophysical fluid problem. Rev. Geophys. Space Phys., *20,* 851–875.

Moody, J. A., B. Butman, R. C. Beardsley, W. S. Brown, P. Daifuku, J. D. Irish, D. A. Mayer, H. O. Mofjelf, B. Petrie, S. Ramp, P. Smith and W. R. Wright. 1984. Atlas of tidal elevation and current observations on the northeast American continental shelf and slope. U.S. Geological Survey Bull., *1611,* 122 pp.

Naimie, C. E. 1996. Georges Bank residual circulation during weak and strong stratification periods: prognostic numerical model results. J. Geophys. Res. *101*(C3), 6469–6486.

Naimie, C. E., J. W. Loder and D. R. Lynch. 1994. Seasonal variation of the three-dimensional residual circulation on Georges Bank. J. Geophys. Res., *99,* 15,967–15,989.

Osborn, T. R. 1980. Estimates of the local rate of vertical diffusion from dissipation measurements. J. Phys. Oceanogr., *10,* 83–89.

Pastuszak, M., W. R. Wright and D. Patanjo. 1982. One year of nutrient distribution in the Georges Bank region in relation to hydrography, 1975–1976. J. Mar. Res., *40,* (Suppl.), 525–542.

Pratt, L. J. 1991. Hydraulics of rotating stratified and sill flow. Ann. Rev. Fluid Mech., *23,* 81–106.

Simpson, J. H., W. R. Crawford, T. P. Rippeth, A. R. Campbell and J. V. S. Cheok. 1996. The vertical structure of turbulent dissipation in shelf seas. J. Phys. Oceanogr., *26,* 1579–1590.

Smolarkiewicz, P. K. 1984. A fully multidimensional positive definite advection transport algorithm with small implicit diffusion. J. Computational Phys., *54,* 325–362.

Smolarkiewicz, P. K. and T. L. Clark. 1986. The multidimensional positive definite advection transport algorithm: further development and applications. J. Computational Phys., *67,* 396–438.

Smolarkiewicz, P. K. and W. W. Grabowski. 1990. The multidimensional positive definite advection transport algorithm: nonoscillatory opinion. J. Computational Phys., *86,* 355–375.

Trowbridge, J. H. and S. J. Lentz. 1991. Asymmetric behavior of an oceanic boundary layer above a sloping bottom. J. Phys. Oceanogr., *21,* 1171–1185.

Werner, S. 1996. The vertical structure of the bottom boundary layer on the southern flank of Georges Bank during later winter. M.S. thesis, MIT/WHOI Joint Program, 135 pp.

Wunsch, C. 1969. Progressive internal waves on slopes. J. Fluid Mech., *35,* 131–144.

Yoshida, J. and N. S. Oakey. 1996. Characterization of vertical mixing at a tidal-front on Georges Bank. Deep-Sea Res., *43,* 1713–1744.

Zimmerman, J. T. F. 1978. Topographic generation of residual circulation by oscillatory tidal currents. Geophys. Astrophys. Fluid Dyn., *11,* 35–47.

—— 1979. On the Euler-Lagrange transformation and the Stokes' drift in the presence of oscillatory and residual currents. Deep-Sea Res., *26A,* 505–520.

Received: *17 June, 1997;* revised: *28 July, 1998.*